

# A search for gravitationally lensed quasars and quasar pairs in Pan-STARRS1: spectroscopy and sources of shear in the diamond 2M1134–2103

Cristian E. Rusu<sup>1</sup>, <sup>1</sup>★† Ciprian T. Berghea,<sup>2</sup> Christopher D. Fassnacht,<sup>3</sup> Anupreeta More<sup>4,5</sup>, Erica Seman,<sup>2</sup> George J. Nelson<sup>2</sup> and Geoff C.-F. Chen<sup>1</sup>

<sup>1</sup>Subaru Telescope, National Astronomical Observatory of Japan, 650 N Aohoku Pl, Hilo, HI 96720, USA

<sup>2</sup>U.S. Naval Observatory (USNO), 3450 Massachusetts Avenue NW, Washington, DC 20392, USA

<sup>3</sup>Department of Physics, University of California, Davis, CA 95616, USA

<sup>4</sup>Kavli IPMU (WPI), UTIAS, The University of Tokyo, Kashiwa, Chiba 277-8583, Japan

<sup>5</sup>Inter-University Centre for Astronomy and Astrophysics, Post Bag 4, Ganeshkhind, Pune 410007, India

Accepted 2019 April 15. Received 2019 March 16; in original form 2018 March 19

## ABSTRACT

We present results of a systematic search for gravitationally lensed quasars in Pan-STARRS1. Our final sample of candidates comprises of 91 systems, not including 25 rediscovered lensed quasars and quasar pairs. In the absence of spectroscopy to verify the lensing nature of the candidates, the main sources of contaminants are likely to be quasar pairs, which we consider to be a byproduct of our work, and a smaller number of quasar + star associations. Among the independently discovered quads is 2M1134–2103, for which we obtained spectroscopy for the first time, finding a redshift of 2.77 for the quasar. There is evidence for microlensing in at least one image. We perform detailed mass modelling of this system using archival imaging data, and find that the unusually large shear responsible for the diamond-like configuration can be attributed mainly to a faint companion  $\sim$ 4 arcsec away, and to a galaxy group/cluster  $\sim$ 30 arcsec away. We also set limits of  $z \sim 0.5$ –1.5 on the redshift of the lensing galaxy, based on its brightness, the image separation of the lensed images, and an analysis of the observed photometric flux ratios.

**Key words:** gravitational lensing: strong – quasars: individual: 2M1134–2103.

## 1 INTRODUCTION

To date,  $\sim$ 60 quadruple (quad) and  $\sim$ 200 double gravitationally lensed quasars have been discovered.<sup>1</sup> Their value as probes of cosmology and astrophysics has been explored observationally for the past four decades (see e.g. reviews by Claeskens & Surdej 2002; Treu & Marshall 2016), yet their number is still a limiting factor for many focused studies (e.g. Oguri et al. 2012; Schechter et al. 2014; Bonvin et al. 2017). We are currently in a post-Sloan Digital Sky Survey (SDSS; York et al. 2000) era when the large ongoing imaging surveys such as the Panoramic Survey Telescope and Rapid Response System (Pan-STARRS1, hereafter PS1; Chambers et al. 2016), the Dark Energy Survey (Flaugher et al. 2015) and the

Hyper Suprime-Cam Subaru Strategic Program (Aihara et al. 2018) do not (yet) have a spectroscopic counterpart, making it difficult to identify lensed quasars. As a result, contemporary dedicated searches for lensed quasars rely on selecting their candidates by applying machine learning techniques such as artificial neural networks (e.g. Agnello et al. 2015) or Gaussian mixture models (e.g. Ostrovski et al. 2017; Williams, Agnello & Treu 2017) to multifilter photometric catalogues in conjunction with pixel-by-pixel pattern recognition; by looking for flux and position offsets between these surveys and *Gaia* (e.g. Lemon et al. 2017; Agnello & Spinelli 2018), including capitalizing on the superior *Gaia* resolution to resolve blended sources (e.g. Agnello et al. 2018b, 2018c; Lemon et al. 2018; Delchambre et al. 2019) and combining multiple such methods (e.g. Spinelli 2018; Lemon et al. 2019); by assessing the plausibility of valid lensing configurations on automatically detected sources (e.g. Chan et al. 2015); and/or by complementing these with variability information (e.g. Berghea et al. 2017; Kostrzewska-Rutkowska et al. 2018).

Encouraged by the serendipitous discovery by Berghea et al. (2017) of the first quad from PS1, PSOJ0147, we have begun

\* E-mail: [cerusu@naoj.org](mailto:cerusu@naoj.org)

† Subaru Fellow.

<sup>1</sup>Lemon, Auger & McMahon (2019) have compiled an up-to-date list of known lensed quasars, maintained at <https://www.ast.cam.ac.uk/ioa/research/lensedquasars/>. Also, C. Lemon, private communication.

a systematic search for lensed quasars in this survey, by cross-correlating sources with the parent active galactic nucleus (AGN) catalogue of Secrest et al. (2015). As the first PS1 data were released in 2016 December, mining it for lensed quasars has only recently begun (e.g. Ostrovski et al. 2018), making it likely that other lensed quasars, including bright, large separation quads, are yet to be found. Given the PS1 sky coverage and depth, Oguri & Marshall (2010) estimate that PS1 contains  $\sim$ 2000 lensed quasars, including 300 quads.

Recently, Lucey et al. (2018, hereafter L18) have announced the discovery of a new bright, large-separation quad, 2M1134–2103. This was a serendipitous discovery, as part of a search for extended 2MASS (Skrutskie et al. 1997) sources in the PS1 footprint, to include as targets for the Taipan Galaxy Survey (da Cunha et al. 2017). As part of our search, we have independently discovered this system. Here, we aim to present a more in-depth modelling of the archival imaging data, looking in particular to identify the cause for the unusually large shear inferred in L18. In addition, we present for the first time spectroscopic data for this system.

The structure of this paper is as follows: in Section 2 we describe our search technique and a new sample of lensed quasars and quasar pair candidates. In Section 3 we describe our analysis of the archival imaging data of 2M1134–2103, and in Section 4 our newly acquired spectroscopic data. In Section 5 we present our mass modelling of 2M1134–2103, and provide plausible explanations for the unusually large shear. We conclude in Section 6. Where necessary, we use a flat cosmology with  $\Omega_\Lambda = 0.74$  and  $h = 0.72$ .

## 2 A SEARCH FOR GRAVITATIONALLY LENSED QUASARS IN PS1

### 2.1 Selection based on catalogue cuts and visual inspection

PS1 is a wide-field imaging system with a 1.8 m telescope and  $7.7 \text{ deg}^2$  field of view, located on the summit of Haleakala in the Hawaiian island of Maui. The 1.4 Gpixel camera consists of 60 CCDs with pixel size of 0.256 arcsec (Onaka & al. 2008; Tonry & Onaka 2008). The first PS1 data release includes both images and a photometry catalogue (Chambers et al. 2016). PS1 uses five SDSS-like filters ( $g_{P1}, r_{P1}, i_{P1}, z_{P1}, y_{P1}$ ). The largest survey PS1 performs is the  $3\pi$  survey, covering the entire sky north of  $-30^\circ$  declination.

As we did for PSOJ0147, we start our search with the AGN candidates catalogue of Secrest et al. (2015), based on two mid-infrared colours measured with the *Wide-field Infrared Survey Explorer* (WISE; Wright et al. 2010). We cross-correlate this catalogue with the PS1 catalogue<sup>2</sup> (Flewelling et al. 2016) using a 3 arcsec radius cone search and keep 79 951 candidates which have at least two counterparts (step *i*). Next, we remove candidates within 15 deg of the galactic plane, resulting in 64 055 remaining sources (*ii*). We then impose a faint magnitude cut of  $i = 19.5$  on the closest counterpart, in order to eliminate spurious candidates. This results in 25 493 sources remaining (*iii*).<sup>3</sup> Finally, we impose

that the two brightest sources in each system should be similar in colour, removing the ones with  $g - i$  differences larger than 1.5 mag and  $i - y$  differences larger than 1.0 mag (*iv*). The final sample contains 18 015 candidates.

We chose these cuts in order to recover most of the known lenses at the intersection of PS1 and the Secrest et al. (2015) catalogue, while resulting in a number of candidates small enough to allow visual inspection. From an all-sky catalogue of  $\sim$ 260 known lenses (Lemon et al. 2019), which we matched with the Secrest et al. (2015) catalogue to insure a match within 10 arcsec, we found 45 lenses for which their Secrest et al. (2015) catalogue counterparts have at least two detections in PS1 within 3 arcsec (corresponding to step *i*). These are further reduced to 44 (*step ii*), 32 (*iii*), and 30 lenses (*iv*).<sup>4</sup> In addition to the cross-match with the known catalogue of lensed quasars, we also looked for previously known non-lens systems, by cross-matching the coordinates of our candidates with the list of known sources from the SIMBAD Astronomical Data base<sup>5</sup> and the NASA/IPAC Extragalactic Data base.<sup>6</sup>

We downloaded  $30 \times 30 \text{ arcsec}^2$  postage stamp colour JPEG images of the candidates using the PS1 cut-out service,<sup>7</sup> which were then inspected visually by three of the authors (CTB, ES, and GJN). Pairs with separation  $\lesssim$ a few arcsec between components (consistent with strong lensing by galaxies) and similar colours, triplets with a redder inner component, as well as quads with configurations consistent with canonical lensing configurations were kept. Finally, another three authors (CER, AM, and GCFC) graded the remaining sample of 448 candidates. As is customary in the lens search community, they used the following grading system: 0: unlikely to be a lens; 1: possibly a lens candidate (satisfies only some criteria to be a lens); 2: probably a lens candidate (satisfies most criteria to be a lens); 3: almost certainly a lens (there is almost no doubt that this is a lens). We find 312 systems with an average grade  $\geq 1$ , and discard the rest.

Out of the 312 candidates, we recover a total of 15 known lenses. Of these, 6 are quads: PS J0147+4630 (Berghea et al. 2017), 2M 1134–2103 (Lucey et al. 2018), SDSS J1433+6007 (Agnello et al. 2018a), GraL J1537–3010 (Delchambre et al. 2019; Lemon et al. 2019), PS J1606–2333 (Lemon et al. 2018), and PS J1721+8842 (Lemon et al. 2018), and 9 are doubles: DES J0245–0556 (Agnello et al. 2018b), PS J0259–2338 (Lemon et al. 2018), HE 1104–1805 (Wisotzki et al. 1993), J1206–2543 (Lemon et al. in preparation), SDSS J1206+4332 (Oguri et al. 2005), SDSS J1320+1644 (Rusu et al. 2013), ULAS J1405+0959 (Jackson et al. 2012), SDSS J1515+1511 (Inada et al. 2014), and J2212+3144 (Lemon et al. 2019). This means that at the grading stage we miss the cluster quad SDSS J1004+4112 (Inada et al. 2003). In addition, at the initial visual inspection stage to produce the list for grading we miss the quad PG1115+080 (Weymann et al. 1980) and 15 doubles: PS J0028+0631 (Lemon et al. 2018), J0102+2445 (Lemon et al. 2019), Q0142–100 (Surdej et al. 1987), PS J0949+4208 (Lemon et al. 2018), SDSS J1001+5027 (Oguri et al. 2005), SDSS J1313+5151 (Ofek et al. 2007), SDSS J1349+1227 (Kayo et al. 2010), SDSS J1442+4055

<sup>2</sup>We use the version available on Vizier, <http://vizier.u-strasbg.fr/viz-bin/VizieR>, which contains fewer contaminants

<sup>3</sup>Following step *iii*, we explored using an additional step to eliminate globular clusters and similar crowded regions, by imposing the condition that there are no more than seven counterparts within 10 arcsec radius. This would have eliminated only 182 systems, all of which we have explored visually, making this step unnecessary.

<sup>4</sup>In addition to these, two other lensed quasars survive our selection and grading process, but are not picked up by the cross-match with the catalogue of lenses because of differences in the reported coordinates: SDSS J1320+1644 and SDSS J1433+6007.

<sup>5</sup><http://simbad.u-strasbg.fr/simbad/sim-fcoo>.

<sup>6</sup><http://ned.ipac.caltech.edu/?q=nearposn>.

<sup>7</sup>[http://hla.stsci.edu/fitscutcgi\\_interface.html](http://hla.stsci.edu/fitscutcgi_interface.html).

(More et al. 2016), ULAS J1527+0141 (Jackson et al. 2012), PS J2124+1632 (Lemon et al. 2018), another double from Ostrovski et al. in preparation and four more doubles from Lemon et al. in preparation.

Our cross-match with known lenses shows that we are more efficient at recovering quads than doubles, which is to be expected, because typical quad configurations are easier to identify visually. We are also biased against large-separation lenses, due to our requirement to have at least two components within 3 arcsec. Since at the visual selection stage we miss 17/32 of the known lenses included in our cut-outs, we expect the completeness of our sample of candidates, defined as the ratio of the number of gravitational lenses in the final sample to the true number of lenses in the cut-outs, to be  $\lesssim 50$  per cent. Most of these are missed at the initial visual inspection stage. This can be attributed to two factors: first, most of the missed systems are doubles with only two clearly visible components in the cut-outs, and with noticeable colour differences between the components. On the other hand, the authors who have inspected the 18 015 candidates have no formal experience with gravitational lenses. When the authors with formal experience graded 11/17 missed lenses, 9 of these received an average grade  $\geq 1$ .

We note that other known quads with bright lensing galaxies, such as 2M1310–1714 (L18), are not included in our sample because the lens light contaminates the infrared colours that the Secrest et al. (2015) AGN catalogue is based on. Secrest et al. (2015) note that the chance of misclassifying stars in the AGN catalogue is  $\leq 0.041$  per cent, so we expect that the main contaminants to our list of candidates, after visual examination, will be quasar + star pairs as well as quasar pairs, as either physically associated binary quasars or projected chance alignments. Indeed, 93 of our candidates, the great majority of those with spectroscopic results in the literature, consist of at least one AGN.

We note that we have typically given a grade of 1 to candidates consisting of object pairs without signs of additional emission, as long as the separation was not too large. This is for two reasons: first, the lensing galaxy may be too faint to detect, which is consistent with the large fraction of known doubles we miss. This fraction would undoubtedly be even higher if we chose to exclude these pairs. Second, because rather than focusing on producing the purest lensed quasar sample, we prefer to include in our sample binary quasars and quasar pairs, which are of interest to the AGN community, for example for studies of quasar triggering (e.g. Hopkins et al. 2008), and of the small-scale quasar–quasar correlation function (e.g. Hennawi et al. 2006; Kayo & Oguri 2012).

## 2.2 Removal of quasar–star pairs using *Gaia*

The recent availability of the *Gaia* mission (Gaia Collaboration 2016), and in particular of its second data release catalogue (DR2; Gaia Collaboration 2018a), has resulted in wide application in the latest searches for lensed quasars, as demonstrated by the multitude of recent studies enumerated in Section 1. Here, we capitalize on the astrometric quantities included in this catalogue in order to further prune our list of candidates.

*Gaia* DR2 includes  $\sim 1.7$  billion sources over the whole sky, with a limiting magnitude of  $G \sim 21$  (Gaia Collaboration 2018a). With a full width at half-maximum (FWHM) of  $\approx 0.1$  arcsec (Fabricius et al. 2016), *Gaia* is effective at deblending close pairs and clusters of objects, down to 0.4 arcsec in DR2 (Arenou et al. 2018). Multi-epoch photometry has enabled the measurement of proper motions and parallaxes for  $\sim 360$  million sources, and the Astrometric Excess

Noise (AEN; Koposov, Belokurov & Torrealba 2017) provides a means of separating compact galaxies from point sources. Colour information ( $Rp - Bp$ ) is also available for  $\sim 1.4$  billion sources.

We have cross-matched our candidates with the *Gaia* DR2 catalogue, in order to identify the counterparts of both PS1 sources in each candidate (up to four sources, in case of quads). Of the 312 candidates, 307 have detections in *Gaia*, 291 of these have measured parallaxes and proper motions, and 283 have measured colours. Of their companions (i.e. the secondary component in the pair of each system, or the brightest secondary component in case of quads), the corresponding numbers are 291, 276, and 260.

We use the proper motion as a classifier, in the form of the proper motion significance defined by Lemon et al. (2019),  $\sqrt{(\text{pm}_{\text{ra}}/\sigma_{\text{pm}_{\text{ra}}})^2 + (\text{pm}_{\text{dec}}/\sigma_{\text{pm}_{\text{dec}}})^2}$ , which includes both celestial coordinates, and where  $\sigma$  stands for the measured uncertainty. We adopt a limiting upper value of 5, which recovers  $\sim 95$  per cent of known lensed quasar images (see fig. 1 in Lemon et al. 2019). For the parallax  $\varpi$ , we use  $\varpi/\sigma_{\varpi} \leq 4$ , corresponding to a  $4\sigma$  limit, since the distribution of measured parallaxes is well approximated by a Gaussian (Gaia Collaboration 2018b). Finally, we use AEN  $\leq 4$ , corresponding to the limit which separates best between lensed quasar images and galaxies, and recovers  $\sim 90$  per cent of the former (see fig. 2 in Lemon et al. 2019).<sup>8</sup>

Our final classification of the 312 candidates is: 91 surviving candidates yet unconfirmed (1 grade A, 4 grade B, and 86 grade C), 25 confirmed systems (6 quads, 9 doubles,<sup>9</sup> 10 quasar pairs), and 196 rejected candidates. We present our final sample of 91 gravitationally lensed quasar and quasar pair candidates in Table 1, together with our comments based on visual inspection and *Gaia* measurements. In Table B1 we also list the already confirmed candidates, as well as the rejected ones. From these tables it can be seen that the proper motion was the dominant classifier for the overwhelming majority of candidates. Finally, Fig. 1 shows that the companions have a similar distribution of *Gaia* colours with the primary sources, but are typically fainter.

## 2.3 Expected sample purity

In addition to the expected completeness, we also wish to estimate the purity of our sample, defined as the ratio of (number of gravitational lenses + quasar pairs)/(total number of sources in the sample). First, we perform a simple exercise where we estimate this number focusing only on the quasar pairs, and comparing the density of sources in a catalogue of point sources, and one of AGN. The idea is to estimate how many of the candidate source companions are expected to be AGN, as opposed to stars. We present the details of the computation in Appendix A. We arrive at a result of  $\sim 4$  per cent.

The expected purity can be computed more directly using the subsample of candidates for which spectroscopic data are available in the literature. Out of 33 candidates which survive the *Gaia*-based cut and which can be either confirmed or ruled out based on the literature, 9 are doubles, 10 are quasar pairs, 6 are quads, and 8 are

<sup>8</sup>Our chosen limits recover almost all of our confirmed candidates: among our 25 spectroscopically confirmed lenses or quasar pairs, only 2, both quads with four detected components in *Gaia*, would be (partially) ruled out based on our *Gaia* classifier: PSJ0147+4630 has one component with large parallax, and PSJ1606–2333 has one with large proper motion.

<sup>9</sup>Note that it is presently unknown whether SDSS J1320+1644, counted here as a double, is in fact a double or a quasar pair (Rusu et al. 2013).

**Table 1.** Sample of gravitationally lensed quasar candidates and quasar pair candidates identified systematically from PS1.

Name (PS1 J...)	$\alpha$	$\delta$	#Comp	$i$	Sep. (arcsec)	Rank	G mags; notes
000815–043634	2.061059	−4.609377	2	18.57	2.4	C	18.82, 20.09; similar colour p-l; both components negligible AEN, p, and pm
003309–120520	8.287252	−12.088925	3	18.10	6.8	C	18.93, 20.38; p-l (both negligible AEN, pm, and p) + red inner component
004106+032726	10.275022	3.457205	2	18.43	2.4	C	18.91, 20.36; p-l; includes SDSS $z = 1.282$ QSO; both negligible AEN, pm, and p
004518+405433	11.325876	40.909217	2	18.69	3.1	C	19.32, 18.85; similar colour p-l; includes $z = 1.228$ QSO (Huo et al. 2013); both negligible AEN, pm, and p
012221+291431	20.587958	29.242069	2	18.30	2.4	C	18.41, 20.72; similar colour p-l; one component negligible AEN, pm, and p; companion has no <i>Gaia</i> pm and p
012256+783855	20.733302	78.648546	2	18.43	2.0	C	18.94, 18.99; similar colour p-l; both negligible AEN, pm, and p
012648+411136	21.698143	41.193204	2	19.13	3.1	C	19.26, 20.15; similar colour p-l; both negligible AEN, pm, and p
013021+072516	22.585897	7.421231	2	18.80	2.0	C	18.98, 19.65; p-l; one component negligible AEN, pm, and p; companion has no <i>Gaia</i> pm and p
014114+062740	25.307825	−6.461006	2	19.05	2.4	C	20.79; similar colour p-l; only one has <i>Gaia</i> data; negligible AEN, pm, and p
014455+271137	26.230638	27.193616	2	19.01	1.9	C	19.53, 19.63; similar colour p-l; both negligible AEN, pm, and p
014912+422843	27.299792	42.478624	2	17.85	2.8	C	17.99, 18.82; similar colour p-l; both AEN, negligible pm and p
015417+433319	28.571648	43.555321	2	18.05	2.7	C	18.92, 18.28; similar colour p-l; both negligible AEN, pm, and p
022205+234144	35.521817	−23.69567	2	18.99	2.1	C	18.96, 20.45; similar colour p-l; both negligible AEN, pm, and p
022958+032031	37.492401	3.341935	2	18.02	2.1	C	18.15, 18.79; similar colour p-l; both negligible AEN, pm, and p
024245+100257	40.688737	−10.049076	2	18.43	2.4	C	18.73, 19.50; similar colour p-l; both negligible AEN, pm, and p
024950+260651	42.459532	26.114096	2	18.56	3.2	C	18.81, 20.15; similar colour p-l; both negligible AEN, pm, and p
042022+01932	65.092136	−10.325513	2	18.54	3.2	B	extended + p-l; no <i>Gaia</i> data
045048+280957	72.701208	−28.165922	2	18.95	5.0	C	18.87, 19.07; similar colour p-l; both negligible AEN, pm, and p
051623+043755	79.096146	−4.631812	2	18.20	3.0	C	18.48, 18.47; p-l; both negligible AEN, pm, and p
052026+045245	80.10733	−4.879078	2	19.30	2.4	C	19.57, 19.65; similar colour p-l; both negligible AEN, pm, and p
052902+032948	82.260144	−3.496646	2	19.27	1.4	C	19.84, 20.37; similar colour p-l; both negligible AEN, pm, and p
061215+193928	93.063509	−19.657707	2	17.49	2.2	C	18.26, 20.34; similar colour p-l (both negligible AEN, pm, and p) + red companion; included in the Delchambre et al. (2019) <i>Gaia</i> clusters catalogue
063019+264851	97.580318	−26.814116	3	18.58	3.4	C	18.99, 19.05, 19.54; p-l; all have negligible AEN, pm, and p; included in the Delchambre et al. (2019) <i>Gaia</i> clusters catalogue
064505+057575	101.269368	50.965199	2	18.84	3.0	C	19.56, 19.14; similar colour p-l; both negligible AEN, pm, and p
064519+380712	101.3227789	38.119957	2	17.3	2.4	B	18.50, 17.63; similar colour p-l; both negligible pm and p
070249+530654	105.704772	53.114994	2	19.05	2.5	C	19.05, 19.65; p-l; both negligible AEN, pm, and p
073017+152842	112.570702	15.4782	2	18.52	2.2	C	19.40, 18.78; similar colour p-l; both negligible AEN, pm, and p
081357+103304	123.486422	10.551007	2	18.62	2.7	C	18.97, 18.70; similar colour p-l; includes SDSS $z = 0.799$ QSO; SQLS candidate; both negligible AEN, pm, and p
081806+524732	124.523269	52.792161	2	17.66	3.3	C	18.96, 17.82; similar colour p-l; includes SDSS $z = 1.793$ QSO; SQLS candidate; both negligible AEN, pm, and p
085254+014850	133.223392	−1.813836	2	18.56	3.2	C	18.51, 19.94; similar colour p-l; both have negligible AEN, pm, and p
090611+093755	136.545112	−9.632052	2	18.76	2.8	C	18.86, 19.66; similar colour p-l; both have negligible AEN, pm, and p
091724+054200	139.348239	−5.700061	2	18.80	2.6	C	18.87, 19.21; similar colour p-l; both have negligible AEN, pm, and p
092823+213853	142.096699	21.647987	2	18.84	2.6	C	19.05, 19.14; similar colour p-l; both have negligible AEN, pm, and p
094450+243476	146.208881	24.382929	2	19.08	2.4	C	19.84, 20.98; p-l; only one component has <i>Gaia</i> pm and p, negligible values
095324+570319	148.351564	57.055364	2	18.70	2.6	C	19.33, 18.90; similar colour; includes SDSS $z = 0.619$ QSO; SQLS candidate, no lensing object; both have negligible AEN, pm, and p

Table 1 – continued

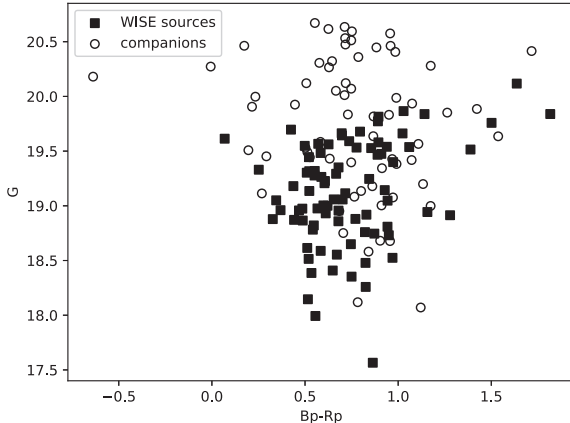
Name (PS1 J...)	$\alpha$	$\delta$	#Comp	$i$	Sep. (arcsec)	Rank	G mags; notes
100406+223132	151.025821	52.525602	2	19.45	2.3	C	similar colour p-l; no <i>Gaia</i> data
100809–044923	152.038129	−4.823158	2	18.56	2.9	C	18.61, 20.14; p-l; only one component has <i>Gaia</i> pm and p, negligible values
110928–233315	167.3666219	−23.554197	2	19.13	2.3	C	19.47, 20.59; similar colour; both have negligible AEN, pm, and p
111524–030727	168.850362	−3.124282	2	18.78	2.6	C	20.12, 19.06; similar colour p-l; both have negligible AEN, pm, and p
112145+011422	170.436445	1.239436	2	19.17	1.5	C	19.35, 19.81; similar colour p-l; includes SDSS $z = 1.292$ QSO; companion has no <i>Gaia</i> p and pm
112456–230507	171.233583	−23.085325	2	19.10	1.8	C	19.48, 19.51; similar colour p-l; both have negligible AEN, pm, and p
113800+073004	174.495987	7.501138	2	18.25	2.8	C	18.39, 19.40; similar colour p-l; includes SDSS $z = 1.209$ QSO; SQLS candidate; no <i>Gaia</i> p and pm
115458+185527	178.740065	18.924205	3	18.83	2.7	C	18.88, 20.31; similar colour p-l (both have negligible AEN, pm, and p) + red component
121410+333703	183.540724	33.617445	3	18.91	2.5	B	19.14, 20.41; similar colour p-l (one component has <i>Gaia</i> data, negligible AEN, pm, and p) + red component; includes SDSS $z = 1.774$ QSO, SQLS candidate
121410+292445	183.541535	29.412494	2	19.47	1.5	C	19.81; similar colour p-l; only one component has <i>Gaia</i> data; negligible AEN, pm, and p
121710–025622	184.290272	−2.939367	2	19.08	1.7	C	19.68; similar colour p-l; includes SDSS $z = 1.465$ QSO (Croom et al. 2001); companion has no <i>Gaia</i> data
121756–181837	184.481806	−18.310394	2	19.42	2.5	C	19.44, 20.45; p-l; both have negligible AEN, pm, and p
130451–102826	196.211716	−10.473908	2	19.00	2.2	C	19.28, 20.14; p-l; both have negligible AEN, pm, and p
130602+210549	196.510055	21.09696	2	18.01	2.1	C	third red component; no <i>Gaia</i> data
132202+030933	200.508342	31.159175	2	19.33	2.7	C	19.32; similar colour; includes SDSS $z = 0.961$ QSO; SQLS candidate; companion has no <i>Gaia</i> data
135425–094103	208.60498	−9.684109	2	19.05	2.1	C	19.77; similar colour p-l; only one component has <i>Gaia</i> data; negligible values of AEN, pm, and p
141855+244107	214.731082	24.685389	2	18.88	4.5	C	19.06, 20.60; similar colour p-l; includes SDSS $z = 0.573$ QSO; (Williams et al. 2017) candidate; companion has no <i>Gaia</i> data
142816+095443	217.065054	9.911986	2	18.63	1.8	C	18.55, 19.67; p-l; includes SDSS $z = 1.467$ QSO; no lens object; both have negligible AEN, p, and pm
143125–044338	217.854924	−4.727349	2	19.30	2.3	C	19.30, 20.10; similar colour p-l; both have negligible AEN, p, and pm
143928–065828	219.867271	−6.974503	2	19.17	2.3	C	19.47, 19.98; similar colour p-l; both have negligible AEN, p, and pm
144446–163241	221.189796	−16.544779	2	18.59	2.0	C	19.34, 18.95; similar colour p-l; both have negligible AEN, p, and pm
145939+162155	224.914314	16.365409	2	18.67	3.5	C	18.88, 20.27; similar colour p-l; includes SDSS $z = 1.569$ QSO; SQLS candidate; both have negligible AEN, p, and pm
151545+004328	228.936742	0.724443	2	18.96	3.5	C	19.51, 19.33; similar colour p-l; both have negligible AEN, p, and pm
151546–032231	228.941104	−3.375202	2	19.31	2.3	C	19.53, 20.23; similar colour p-l; both have negligible AEN, p, and pm
152841+393229	232.169429	39.541466	2	19.46	1.9	C	19.61, 20.35; similar colour p-l; includes SDSS $z = 1.215$ QSO; both have negligible AEN, p, and pm
153808–192310	234.555305	−19.386104	2	19.29	2.8	C	19.54, 20.43; p-l; both have negligible AEN, p, and pm
162900–140856	247.247099	−14.148889	2	18.55	2.4	C	19.76, 19.00; similar colour; both have negligible AEN, p, and pm
162903+372433	247.260887	37.409037	2	19.05	4.3	C	19.18, 19.40; similar colour p-l; includes SDSS $z = 0.926$ QSO, no lensing object; both have negligible AEN, p, and pm
164556+402246	251.482344	40.379443	2	19.01	2.3	C	19.23; similar colour p-l; one component has negligible AEN, p, and pm, the other has no <i>Gaia</i> data
165831+141605	254.627587	14.268089	2	18.73	2.2	C	19.11, 19.08; similar colour p-l; companion has no <i>Gaia</i> data
170402+115730	256.009503	11.958322	2	18.59	2.9	C	18.75; similar colour p-l; includes SDSS $z = 1.512$ QSO; SQLS candidate; both have negligible AEN, p, and pm
172406+640711	261.027058	64.119668	2	18.16	2.4	C	negligible AEN, p, and pm
172751+194436	261.960528	19.743295	2	19.32	1.9	C	20.11; similar colour p-l; companion has negligible AEN, p, and pm; no <i>Gaia</i> data for main component
175526+631504	268.857193	63.251051	2	19.28	2.2	C	19.66, 19.74; similar colour p-l; both components have negligible AEN, p, and pm
175918+345928	269.825014	34.991208	2	19.09	2.3	C	19.21, 19.64; similar colour p-l; both components have negligible AEN, p, and pm

Table 1 – continued

Name (PS1 J...)	$\alpha$	$\delta$	#Comp	$i$	Sep. (arcsec)	Rank	$G$ mags; notes
183230+534914	278.123646	53.8206	2	19.13	3.0	C	19.58, 20.15; similar colour p-l; both components have negligible AEN, p, and pm
184624+352002	281.599148	35.333764	2	19.33	2.4	C	19.29, 19.76; similar colour p-l; both components have negligible AEN, p, and pm
192808+553219	292.032689	55.538539	2	18.05	2.7	C	19.00, 18.32; similar colour p-l; both components have negligible AEN, p, and pm
195243–111715	298.179179	–11.28742	2	19.46	2.3	C	19.70, 20.32; similar colour p-l; both components have negligible AEN, p, and pm
204258–273754	310.739743	–27.631602	2	19.15	2.3	C	19.14, 20.47; similar colour p-l; both components have negligible AEN, p, and pm
205006–225929	312.523434	–22.991253	2	18.93	2.3	C	19.00, 20.22; similar colour p-l; both components have negligible AEN, p, and pm
205143–111444	312.931008	–11.245566	3	18.95	3.2	A	19.66, 19.93, 20.74; p-l sources in quad-like configuration. Two components have negligible AEN, p, and pm, another has negligible AEN and no other <i>Gaia</i> data; the final one has no <i>Gaia</i> data <sup>a</sup>
212028+280324	320.116547	28.056796	2	18.65	2.9	C	18.78, 19.41; similar colour p-l; both components have negligible AEN, p, and pm
213736+201517	324.398524	20.254669	2	19.29	1.6	C	19.64, 19.66; similar colour p-l; both components have negligible AEN, p, and pm
214132+82621	325.382786	18.439197	2	18.97	2.4	C	18.96, 19.65; similar colour p-l; both components have negligible AEN, p, and pm
214223+255423	325.654002	25.906285	2	18.81	2.9	B	18.76; similar colour p-l; only one component has <i>Gaia</i> data, negligible AEN, p, and pm
214315+075120	325.810482	7.855534	2	18.18	2.7	C	18.52, 19.00; similar colour p-l; both components have negligible AEN, p, and pm
215034–265214	327.643528	–26.870639	2	16.95	1.8	C	includes $z = 0.115$ (lensing?) galaxy (Jones et al. 2009); no <i>Gaia</i> data
215158+111102	327.99043	11.183861	2	18.77	2.6	C	19.06, 19.74; similar colour p-l; includes SDSS $z = 1.797$ QSO; SQLS candidate; both have negligible AEN, p, and pm
220943+043217	332.428196	4.538084	2	18.18	2.9	C	18.59, 18.40; similar colour p-l; both have negligible AEN, p, and pm
222108+214518	335.2828056	21.754907	2	17.34	3.5	C	17.57; different colour p-l; only the main component has <i>Gaia</i> data, negligible AEN, p, and pm
230339+345343	345.91142	34.895107	3	18.36	7.1	C	18.65, 18.98; similar colour p-l (both have negligible AEN, p, and pm) + inner red source
231813+025028	349.554123	2.841082	2	19.31	3.2	C	19.59, 19.43; similar colour p-l; both have negligible AEN, p, and pm
232223+375439	350.595174	37.910703	2	19.23	2.2	C	19.87, 20.81; p-l; both have negligible AEN, p, and pm
232449–122555	351.205773	–12.432025	2	18.93	1.8	C	19.25; p-l; only one component has <i>Gaia</i> data, negligible AEN, p, and pm
233525+184309	353.85286	18.71912	2	19.31	1.9	C	red components; no <i>Gaia</i> data

Here  $\alpha$  and  $\delta$  are the right ascension and declination of the candidates in the International Celestial Reference System. '#Comp' refers to the number of components, where we use the number of PS1 sources inside 3 arcsec radius, but revise it based on visual inspection, removing spurious sources and counting additional objects which appear to be part of the system. The measured separation ('Sep.', in arcsec) is that between the lens candidate point sources or, in case of a quad, the maximum separation between any of the point sources, taken from the PS1 catalogue, or revised as described above. The magnitude is given in  $i$  band in the AB system for the brightest resolved component. We quote the iMeanPsfMag measurements from the PS1 catalogue, or the SEXTTRACTOR (Bertin & Arnouts 1996) MAG\_AUTO in case we had to manually add the brightest component of the system, as described above. We also quote the *Gaia*  $G$ -band magnitudes for each system, in the order of increasing separation from the WISE source coordinates. Here 'p-l' stands for 'point-like', whereas 'AEN' (astrometric excess noise), 'p' (parallax), and 'pm' (proper motion) are *Gaia*-based measurements. We list in this table the alphabetic ranking as gravitationally lensed quasars for all systems with an average grade of 1 and above, based on three human graders, as detailed in Section 2. We follow the following convention for the alphabetic ranking: A: average grade  $> 2.5$ ; B: average grade  $> 1.5$ ; C: average grade  $\geq 1$ . SQLS spectra were searched inside Data Release 14 (Abolfathi et al. 2018).

<sup>a</sup>After the first draft of this work (arXiv:1803.07175v1), this system was independently announced by Delchambre et al. (2019) as a candidate. Our GLAFIC modelling of the observed configuration with an SIE+ $\gamma$  mass profile results in a perfect fit, but the model is underconstrained because the lensing galaxy is not detected.



**Figure 1.** *Gaia* colour–magnitude plot of the main sources and companions with available colours, from the 91 surviving candidates.

galaxy + other, star + other, or star + QSO (here ‘other’ stands for non-QSO). For systems with  $G \leq 20$  for all components (the limit at which *Gaia* is still relatively complete), these numbers are 7, 9, 5, and 5, respectively. This means that for  $G \leq 20$ , if we ignore the quads (there is only one quad candidate in our final sample, and these systems are much easier to identify visually, leading to different selection), the purity for quasar pairs is  $9/21 \approx 43$  per cent, and for doubles + quasar pairs it is  $16/21 \approx 76$  per cent. Of course, care must be taken in interpreting this result, as the spectroscopic selection of these sources compiled from the literature is unknown.

How can the discrepant results of the two methods be reconciled? This is likely due to the known clustering of quasars, which leads to a significant enhancement of small-separation quasar–quasar pairs over expectations from uniform spatial distribution assumptions and catalogue density comparisons, and it means that the number we computed with that method must be interpreted as a lower limit. The quasar–quasar correlation function is predicted to produce an enhanced by a factor of  $\sim 100$  on small angular scales corresponding to quasar pairs (e.g. Peng et al. 1999, and references therein). For our 91 candidates and confirmed quasar pairs we measure a median separation of 2.4 arcsec, with a standard deviation of 0.53 arcsec (after removing four systems with separation  $> 4.5$  arcsec). Kayo & Oguri (2012) do indeed estimate an increase by a factor of  $\sim 200$  in the number of quasar pairs with separation typical for our candidates (physical scale  $\sim 20$  kpc), over the random expectation, based on a sample of binary quasars obtained as a byproduct of a search for gravitationally lensed quasars (Oguri et al. 2006; Inada et al. 2012). This is more than enough to explain the discrepancy. In fact, multiplying this number with the fraction of AGN to point sources found in our simple exercise suggests a purity of  $\sim 90$  per cent. This may be an overestimate, as there is a known discrepancy between the large number of predicted binary quasars (e.g. Hopkins et al. 2006) and the smaller number of discovered ones (e.g. Hennawi et al. 2010). We adopt as our best estimate of the purity the  $\sim 76$  per cent value measured above for quasar pairs + doubles, although we caution that this estimate might be biased due to the unknown spectroscopic selection, and applies only to  $G \leq 20$ . If we remove the magnitude cut, based on the spectroscopic sample, this becomes  $\sim 70$  per cent.

In the following sections, we focus on modelling the imaging and spectroscopic data of 2M1134–2103.

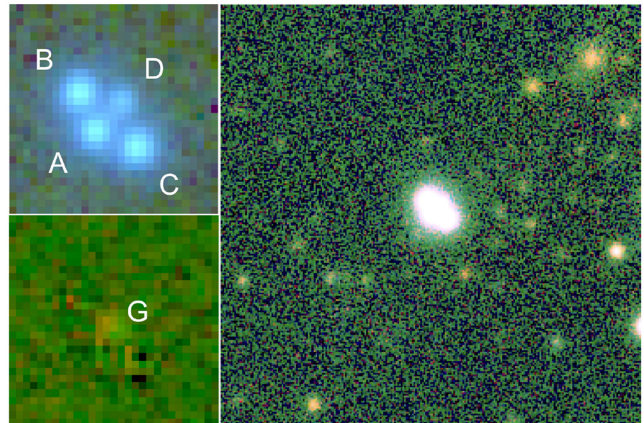


**Figure 2.** *Upper left:* Colour composite (VHS-YJKs) of 2M1134–2103 showing the four lensed quasar images (A, B, C, and D). Image is 10 arcsec on the side. *Lower left:* The same colour composite, after subtracting the four quasar images with HOSTLENS, shows the presence of a lensing galaxy G. *Right:* Colour composite (riz) using PS1 data shows the immediate environment of the lens system, which is located at the centre. Image is 60 arcsec on the side. All images are oriented such that North is up and East is to the left.

### 3 2M1134–2103: IMAGING DATA REDUCTION AND MODELLING

2M1134–2103 consists of four point-like lensed quasar images and a lensing galaxy (see Fig. 2). The lensing galaxy 2M1134–2103 can be convincingly identified in the near-infrared imaging (particularly Ks-band) from the VISTA Hemisphere Survey (hereafter VHS; McMahon et al. 2013, see also Fig. 2). While the relative astrometry of the quasar images, measured from VST-ATLAS (Shanks et al. 2015), is reported in L18, the VST-ATLAS data are not publicly accessible. Furthermore, the VST-ATLAS data have better seeing (0.72 arcsec) but the PS1 data are deeper. Therefore, we make use of archival PS1 data in our analysis. The processing of the archival PS1 data (Flewelling et al. 2016) is described in Magnier et al. (2016a), and includes removal of the instrumental signature, image coaddition, as well as photometric and astrometric calibration (Magnier et al. 2016b). Here, we model the PS1 grizy and VHS YJKs images independently of L18.

For our detailed modelling of 2M1134–2103 we downloaded from the PS1 and VHS archives  $180 \times 180$  arcsec $^2$  cut-outs around the system in all available filters, large enough to contain stars to model the PSF and to improve the image orientation. We subtracted the sky background from the VHS images using SExtractor (Bertin & Arnouts 1996), and resampled all images with SWARP (Bertin et al. 2002) to a common orientation. We measured final pixel scales with SCAMP (Bertin 2006).

We model the system with HOSTLENS (Rusu et al. 2016). HOSTLENS models an arbitrary number of point-like and extended sources using a common point spread function (PSF), either specified by the user from nearby stars, or fitted to the data as a sum of two concentric Moffat (Moffat 1969) profiles. We find that modelling the quasar images using nearby stars as PSFs results in significant residuals, which could affect the image flux measurements and the characterization of the lensing galaxy. We therefore model the data using an analytical PSF fitted to the data. To remove residuals still remaining at the centres of the three bright quasar images in the rizYJKs bands, we use the PSF reconstruction technique described in Chen et al. (2016), with the best-fitting analytical PSF as a starting

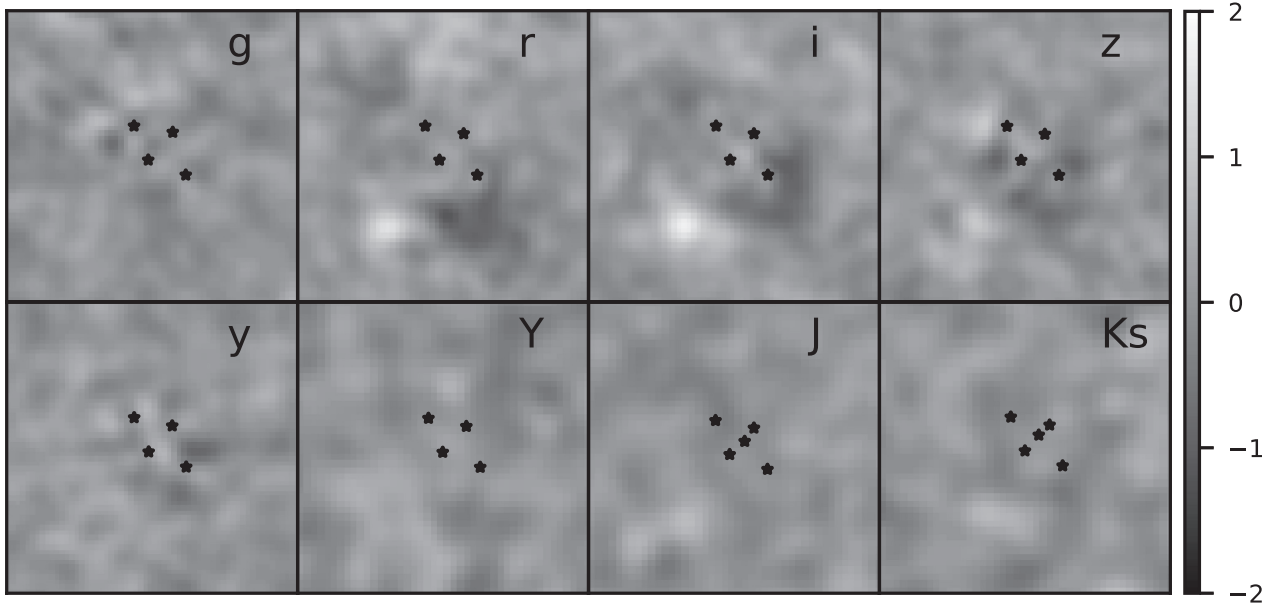


**Figure 3.** Residuals after morphological modelling of imaging data with HOSTLENS. The size of the cutouts is  $15 \times 15$  arcsec $^2$ . The images were divided by the associated noise maps, then smoothed with a 3-pixel Gaussian, to enhance structure. The positions of the components that were modelled in each band (A, B, C, D, as well as G in  $JK_s$ ) are marked with star symbols. Object GX to the south-east of the lens, conspicuous in the  $r$  and  $i$  bands, is left unmodelled (see Section 5).

point. This technique reconstructs the PSF iteratively, on a grid of pixels, under the assumption that the PSF does not vary across the quasar images. The remaining residuals at the location of the quasar images are small, as can be seen in Fig. 3.

In the PS1 data we do not detect any sign of the lensing galaxy, which however stands out in the VHS  $J$  and  $K_s$  images. We model its light profile in these bands simultaneously with the quasar images, using a de Vaucouleurs (de Vaucouleurs 1948) profile commonly used for early-type lensing galaxies. A circular profile fits the emission from the lensing galaxy well, without leaving noticeable residuals. Using a Markov Chain Monte Carlo (MCMC) approach, we find that the lensing galaxy flux is highly degenerate with the effective radius of the de Vaucouleurs profile, and is therefore unreliable.

In order to perform gravitational lens modelling of 2M1134–2103 we need to estimate reliable relative astrometry for the quasar images and the lensing galaxy. For the three brightest quasar images we take the mean and scatter between the measured relative astrometry in different filters (excluding  $g$  band, where the seeing is significantly larger, see Table 2), whereas for the lensing galaxy and the faint counterimage D, we only use the  $J$  and  $K_s$  filters. Indeed, the separation between the brighter images (A, B, and C) and the fainter counterimage (D) decreases slightly with increasing wavelength in the PS1 images, because of the progressively increasing flux contribution from the red lensing galaxy. We report our measured astrometry and photometry in Table 2. Our astrometry is consistent with the one presented in L18 within our  $2\sigma$  uncertainties.

#### 4 2M1134–2103: KECK SPECTROSCOPY

The 2M1134–2103 lens system was observed with the Echelle Spectrograph and Imager (ESI; Sheinis et al. 2002) on the night of 2017 November 18 UT (program number 2017B\_U110). The observations utilized a slit with a width of 1 arcsec and the cross-

dispersed Echelle mode of the spectrograph, which provides a constant dispersion of roughly  $11.5 \text{ km sec}^{-1}$  pix $^{-1}$  over a wavelength range of approximately  $3900$ – $11\,000$  Å. Here, we follow the nomenclature of L18. Two slit position angles were used, one oriented at  $+46.7$  deg (N through E) in order to go across lensed images B and C (henceforth the ‘BC slit’) and one oriented at  $-42.3$  deg to cover images A and D (the ‘AD slit’). We obtained three 600 s exposures through the BC slit and four 600 s exposures through the AD slit.

We calibrated the data using a custom pipeline written in PYTHON. The pipeline does a flat-field correction, rectifies the two-dimensional spectra, does the wavelength calibration using both arc lamp and night sky emission lines, and subtracts the sky emission. The calibrated data for both slits are shown in Fig. 4. In the AD slit, the two-dimensional spectra show one bright trace that is heavily blended with a much fainter trace, while the BC slit shows three clearly separated traces. We identify the three traces in the BC slit with components B, A+D+G, and C in the imaging data. Based on the imaging, we expect that the emission from image A completely dominates the central trace.

We extracted one-dimensional spectra from the exposures on both slits using a second Python pipeline that extracts the spectra from each spectral order, applies a response correction based on observations of a spectrophotometric standard, in this case Feige 110, and finally combines the data from each of the 10 spectral orders into one final spectrum. For the AD slit, we only extracted one aperture that we identify with a blend of A, D, and G, while for the BC slit we extracted separate apertures corresponding to B, A+D+G, and C. Note that the AD slit may very well contain significant scattered light from images B and C. The extracted spectra are shown in Fig. 5 and all show clear broad emission lines that, furthermore, are indicative of quasars at a redshift of  $z_{\text{src}} \sim 2.77$ . Thus, the ESI spectra are fully consistent with the interpretation of 2M1134–2103 as a quad lensed quasar. An exact value of the source redshift is difficult to obtain due to the fact that

**Table 2.** Relative astrometry and absolute photometry of 2M1134–2103.

Filter (lim. mag)	A	B	C	D	G	GX	Seeing (arcsec)
all (x-axis)	0.000 ± 0.000	-0.733 ± 0.005	1.944 ± 0.006	1.262 ± 0.014	0.74 ± 0.04	-2.50 ± 0.05	
all (y-axis)	0.000 ± 0.000	1.757 ± 0.006	-0.776 ± 0.006	1.350 ± 0.020	0.75 ± 0.10	-3.32 ± 0.05	
<i>g</i> (24.2)	17.08 ± 0.005	17.37 ± 0.005	17.26 ± 0.005	18.90 ± 0.014	-	-	1.70
<i>r</i> (24.5)	16.85 ± 0.005	17.06 ± 0.005	17.00 ± 0.005	18.67 ± 0.005	-	[23.37 ± 0.10]	1.20
<i>i</i> (24.5)	16.81 ± 0.005	16.88 ± 0.005	16.83 ± 0.005	18.46 ± 0.005	-	[21.75 ± 0.08]	1.20
<i>z</i> (23.6)	16.87 ± 0.005	16.90 ± 0.005	16.87 ± 0.005	18.49 ± 0.006	-	-	1.10
<i>y</i> (22.6)	16.79 ± 0.04	16.72 ± 0.03	16.70 ± 0.03	18.29 ± 0.04	-	-	1.00
<i>Y</i> (22.2)	16.08 ± 0.008	15.98 ± 0.007	16.02 ± 0.007	17.57 ± 0.016	-	-	0.85
<i>J</i> (21.4)	15.92 ± 0.005	15.81 ± 0.005	15.83 ± 0.005	17.35 ± 0.012	[19.05 ± 0.12]	-	0.85
<i>Ks</i> (20.1)	15.34 ± 0.006	15.13 ± 0.006	15.19 ± 0.009	16.81 ± 0.027	[17.33 ± 0.09]	-	0.85

Relative astrometry is determined by using information from multiple filters (see Section 3). The units are in arcsec and the sign convention is positive from E to W (x-axis) and from S to N (y-axis). The ICRS position of image A in the PS1 catalogue is (J2000.0) 11:34:40.588–21:03:23.06. Magnitudes are in the AB (*grizy*) and Vega (*YJKs*) systems, and are corrected for Galactic extinction following Schlafly & Finkbeiner (2011). The  $1\sigma$  limiting magnitudes are computed in 2 arcsec-radius blank sky apertures around the system. The errors on magnitudes are those from MCMC, with the minimum uncertainty boosted to 0.005 mag, and do not include zero-point or PSF uncertainties. The magnitudes of G and GX (see Section 5) should be considered unreliable, as in order for the fit to converge, the effective radius was fixed to  $<1$  pixel.

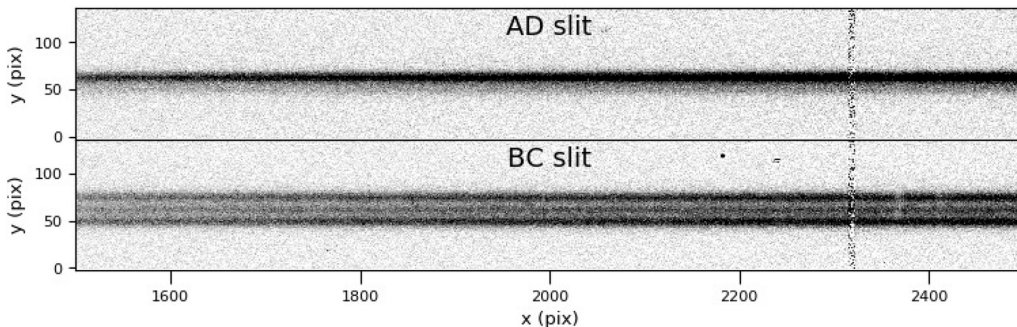


**Figure 4.** Examples of the calibrated and sky-subtracted spectra obtained with Keck/ESI of 2M1134–2103. Data are from the AD slit (top) and the BC slit (bottom), with spectra showing a portion of the fifth of ten spectral orders recorded by the spectrograph.

the peaks of the lines used for redshift determination are affected by absorption systems (Fig. 5; also e.g. Lee 2018). The measured redshift is smaller than the  $z \sim 3.5$  estimate in L18, based on PS1 colours.

In addition to the broad emission lines, all of the spectra show a number of absorption lines. In the range 5000–7500 Å, these correspond to absorption features of Fe and Mg, and are consistent with two separate absorption systems at  $z_{\text{abs},1} = 1.554$  and  $z_{\text{abs},2} = 1.481$ . The first system has stronger lines in the A+D+G and B spectra, while the second is stronger in the image C spectrum. Although it is possible that these systems may be associated with the primary lensing galaxy, the narrowness of the lines makes this interpretation unlikely. A much stronger indication of the lensing galaxy would be the detection of stellar absorption lines, such as the Ca II H and K lines, with widths consistent with the velocity dispersions of  $>100$  km s $^{-1}$  expected for a massive lensing galaxy. If these corresponded to the redshifts of the absorption features mentioned above, they would be observed at wavelengths longer than the ones plotted in Fig. 5, where we have extracted robust spectra.

## 5 2M1134–2103: GRAVITATIONAL LENS MODELLING

We perform gravitational lens mass modelling of 2M1134–2103 with GLAFIC (Oguri 2010), using the observed relative positions

of the quasar images and the lensing galaxy as constraints. We do not impose constraints based on the flux ratios, as these might be affected by microlensing, extinction, and intrinsic variability (e.g. Yonehara, Hirashita & Richter 2008). However, we analyse the observed flux ratios under the assumptions that they are dominated by extinction, in Section 5.1.

We start with the same mass model used in L18, a singular isothermal sphere with external shear (SIS+ $\gamma$ ). This model has  $\chi^2/\text{d.o.f.} = 7.5/3$  (where d.o.f. stands for degrees of freedom), most of which is due to the difference between the measured and predicted position of image D relative to the lens G. We recover the results of L18, in particular that an unusually large shear of  $\sim 0.34$  at 44 deg W of N is required to fit this system.

Secondly, we fit a model which allows for mass ellipticity, SIE+ $\gamma$ . Indeed, quads have enough constraints to disentangle internal and external sources of shear, and our fit shows a dramatic improvement to  $\chi^2/\text{d.o.f.} = 0.1/1$ . This model requires a shear of  $\sim 0.39$ , slightly larger than before, and a mass axial ratio of  $0.80^{+0.10}_{-0.18}$ , with the long axis at  $37^{+5}_{-13}$  deg E of N, almost perpendicular to that of the shear. While our imaging data does not have sufficient resolution to fit an elliptical light profile to the lensing galaxy, studies of quads show that the mass and light profiles of lensing galaxies are typically aligned (e.g. Keeton, Kochanek & Falco 1998; Sluse et al. 2012). We note that Rusu & Lemon (2018) modelled a different quad, GraL J1817+2729, in a cross-like configuration, and showed that while an SIE+ $\gamma$  model required large shear and large ellipticity,

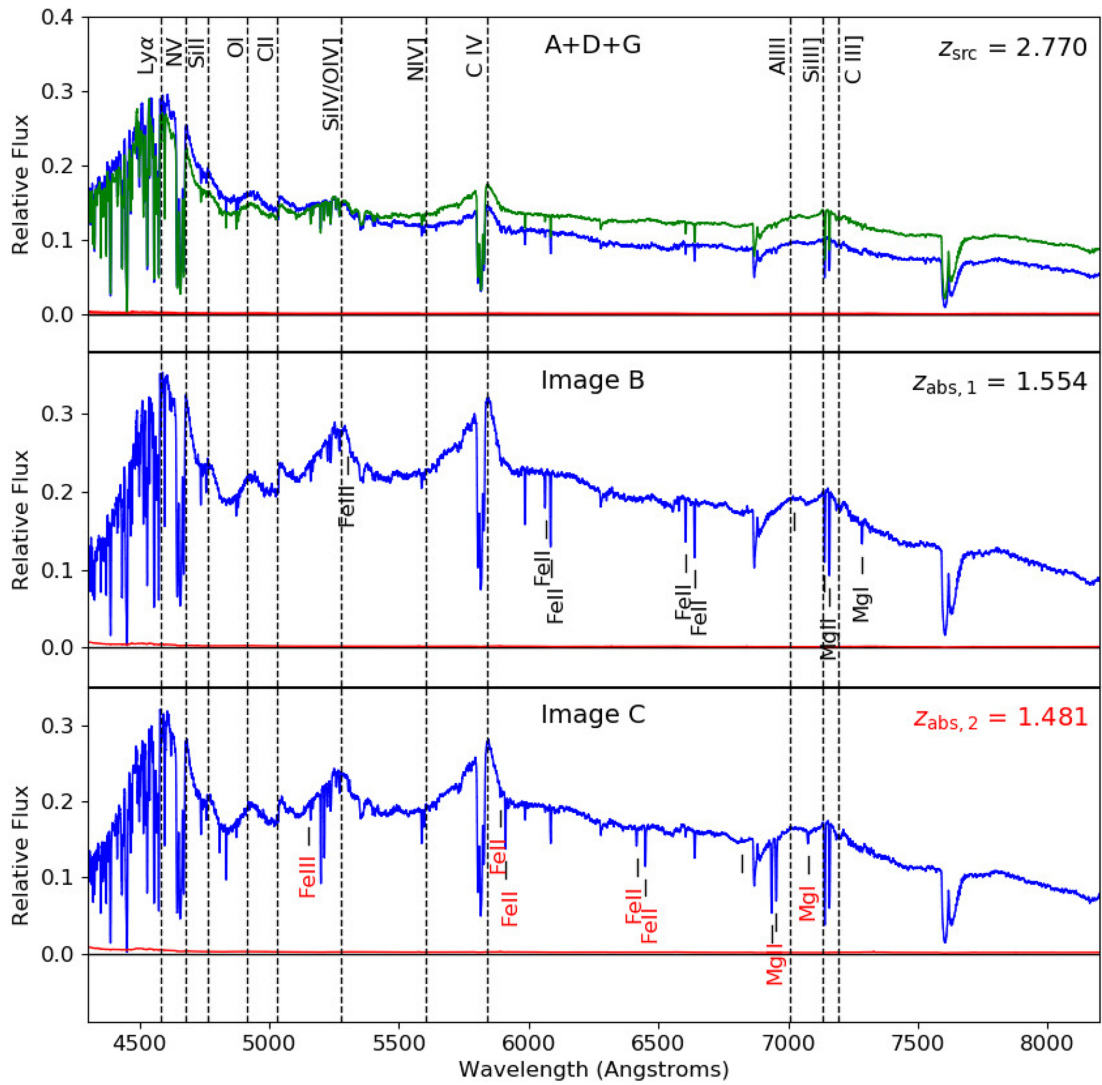


**Figure 5.** ESI spectra of 2M1134–2103. Combined light from lensed images A and D, plus any emission from the lensing galaxy is visible in the spectrum extracted from the AD slit (green) as well as that from the BC slit (dark blue) in the top panel. Spectra of images B (middle) and C (bottom) are extracted from the BC slit. The rms noise of each spectrum is plotted in red. Identified emission and absorption systems are labelled (see further explanation in Section 4). The wide absorption doublet at  $\sim 7650 \text{ \AA}$  is telluric. The spectra were smoothed using a 3-pixel boxcar with inverse-variance weighting.

with the long axis perpendicular to the shear, similar to the present case, a Sersic+SIS+ $\gamma$  model, where the Sersic component stands for the baryonic matter in the disc of the lensing galaxy, significantly diminishes the required shear, and changes its orientation. We attempted to fit such a model here, but it behaves equivalently to our SIE+ $\gamma$  model, requiring similar orientation and large shear. It appears that the highly stretched, diamond-like configuration, cannot be explained by internal sources of shear.

As both the SIS+ $\gamma$  and SIE+ $\gamma$  models are consistent in their requirement of large external shear, we look for potential sources of shear from the surrounding environment. In Fig. 2 we display a  $60 \times 60$  arcsec $^2$  colour composite image around 2M1134–2103, which clearly shows a group of red galaxies in the upper right corner, the brightest of which is a  $i = 19.32$  galaxy located at  $\alpha = 173.6620$ ,  $\delta = -21.0502$ , 30 arcsec from the quad, in the direction of 45 deg W of N. The PS1 and VHS colours of this galaxy imply a photometric redshift of  $0.70 \pm 0.09$ , estimated with BPZ (Benítez 2000). The existence of the galaxy group at this location implies that it is responsible for part of the measured shear. However this is unlikely

to be the complete picture, as an SIS profile at the location of this galaxy would require a very large velocity dispersion  $\gtrsim 1100 \text{ km s}^{-1}$  to produce the measured shear, depending on the redshift of the lensing galaxy in 2M1134–2103.

Fig. 3 reveals another clue, closer to 2M1134–2103. After subtracting the quasar images, an additional component is detected in filters  $r$  and  $i$ , 4.16 arcsec from image A, also in the direction of the shear, towards south-east. It is unclear whether this new component, which we name GX, is a galaxy or a star, as it is too faint ( $i \sim 21.75$ ) to constrain its morphology. Under the assumption that it is a galaxy, its colours suggest a redshift lower than the one of the lensing galaxy, which is only detected in the near-infrared VHS filters. We incorporate GX into a third lensing model, in order to estimate its effect on the external shear. As we do not know the redshifts for either G or GX, we consider the simplest case in which G and GX are modelled as SIS of equal strength, at the same redshift. This model is expected to be an upper limit to the contribution of GX to the lensing configuration, as GX is likely a lower redshift, low-mass galaxy. We obtain a good fit with  $\chi^2/\text{d.o.f.} = 2.3/3$ , and a residual

**Table 3.** Summary of the best-fitting parameter values of the lensing mass models, and the predicted time delays.

Model	$z$	$\sigma$ (km s $^{-1}$ )	$e$	$\theta_e$	$\gamma$	$\theta_\gamma$	$\Delta CA$	$\Delta CB$	$\Delta CD$
SIS+ $\gamma$	0.45	243.0	–	–	0.34	43.6	30.5	6.8	54.8
SIS+ $\gamma$	1.50	384.1	–	–	0.34	43.6	196.6	43.9	353.1
SIE+ $\gamma$	0.45	242.1	0.33	–39.9	0.39	45.2	24.7	6.3	43.6
SIE+ $\gamma$	1.50	382.6	0.33	–39.9	0.39	45.2	159.0	40.3	281.0
2SIS+ $\gamma$	0.45	233.3	–	–	0.19	45.8	33.9	7.5	44.3
2SIS+ $\gamma$	1.50	363.4	–	–	0.19	45.8	225.9	49.3	263.4

Here  $z$  is the lens redshift,  $\sigma$  is the lens velocity dispersion,  $e$  and  $\gamma$  are the lens ellipticity and shear, respectively, and  $\theta_e$  and  $\theta_\gamma$  are their orientations (W of N). The time delays (last column) are in units of days.

external shear of  $\sim 0.19$ , oriented as before. In this model, the two lenses are located  $\sim 4$  Einstein radii apart, in units of the Einstein radius of G. Our model shows that GX can explain a significant fraction of the shear we measured in our initial SIS+ $\gamma$  model. We expect that in reality most of the measured shear is an interplay between the effects of GX and the nearby group. In our model incorporating GX, the nearby group would still require a velocity dispersion of  $\sim 800$  km s $^{-1}$  to account for the remaining shear, which would imply  $\gtrsim 50$  group/cluster members (e.g. Berlind et al. 2006). While we do not see more than  $\sim 3$  possible galaxy members in the PS1 image, this is not an argument against the existence of this structure, as the PS1 images are shallow. Indeed, PS1 images of the system RX J0911+05 reveal only  $\sim 5$  galaxies part of a spectroscopically confirmed cluster with at least 24 members at a similar redshift of  $z = 0.769$ , with velocity dispersion  $\sim 800$  km s $^{-1}$  (Kneib, Cohen & Hjorth 2000), giving rise to a very large shear  $\gtrsim 0.3$  (Sluse et al. 2012).

We note that another lensed system with a remarkably similar diamond-like configuration has recently been discovered (Bettoni et al. 2019) close to a galaxy cluster, also with a large measured shear of 0.31 and a nearby galaxy in the direction of the shear. Finally, we note that highly sheared quadruple lens systems are not unexpected, and are a consequence of the tendency of elliptical galaxies, which constitute most of the lensing galaxies, to reside in overdense regions with high shear (e.g. Holder & Schechter 2003). We conclude that the large shear values we measure do not therefore point out to a problem with our mass models.

In the analysis above we did not assume particular values of source and lens redshifts, except when we estimated the velocity dispersion of the galaxy group at  $z \sim 0.7$ . The flux ratios are also insensitive to the choice of redshifts, however the estimated time delays depend on them. To estimate the time delays, which are of interest to cosmography studies (e.g. Bonvin et al. 2017), we use the source quasar redshift  $z_s = 2.77$  measured from spectroscopy, and the lens redshift limits we infer below in Section 5.1,  $z_l \sim 0.45 - 1.5$ . For  $z_l \sim 0.45$  and the SIS+ $\gamma$  model, the estimated time delays are  $\Delta CB \sim 7$  d,  $\Delta CA \sim 30$  d, and  $\Delta CD \sim 55$  d. The order of the image time arrival is the same in all three models, with image C leading. We summarize the main parameters of the mass models we employed in Table 3, along with the corresponding time delays.

### 5.1 Flux ratio analysis and the lens redshift

We show the measured image flux ratios in Fig. 6, based on Table 2. At least three of the six ratios show a clear dependence on wavelength. Interpreted as due to extinction, these ratios imply that A is the least reddened image, in agreement with image D being closest to the lensing galaxy, and the major axis of the lensing galaxy

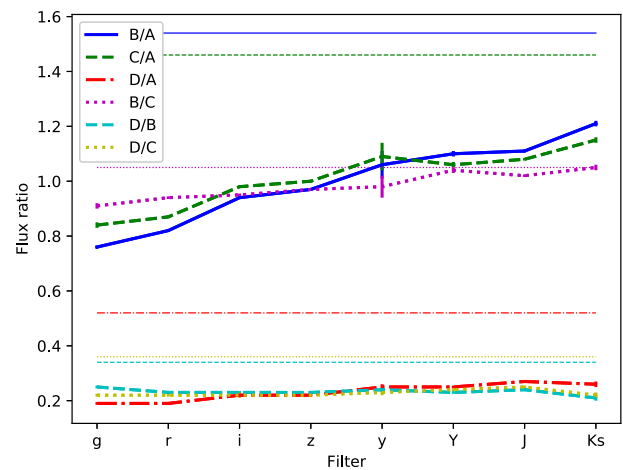


**Figure 6.** Measured and model-predicted flux ratios of the four quasar images. Thick lines connect observed flux ratios in all available filters, and thin horizontal lines of corresponding colours mark the flux ratios predicted by the SIS+ $\gamma$  lens mass model.

being oriented towards B and C (with B more reddened than C), according to the SIE+ $\gamma$  model. We also show in Fig. 6 the predicted flux ratios given by the SIS+ $\gamma$  model. The predicted SIE+ $\gamma$  fluxes are very similar, within  $\sim 10$  per cent, but the G+GX+ $\gamma$  model predicts a demagnified image A, about as bright as D. All models predict image B to be the brightest, as observed in the VHS data. The predicted B/C is invariant across all three models, as the shear is almost perpendicular to the direction of these two images. In fact, this ratio is the only one which matches the observations, in the reddest filter.

Flux ratios of quasar images have been used in the past to study the extinction properties of lensing galaxies (e.g. Falco et al. 1999) as well as to infer lens redshifts (e.g. Jean & Surdej 1998). Here, we use them to infer the lens redshift  $z_l$  as well as the de-reddened flux ratios (relative magnifications)  $M_i$ , where  $i$  refers to each of the six image pairs, independent of the chosen mass model. Following Falco et al. (1999), we optimize these parameters as well as the differential extinctions  $E_i$  and the shape of the extinction curve  $R$  by minimizing

$$\chi^2 = \sum_{j=1}^{N_\lambda} \sum_{i=1}^{N_{\text{imag}}} \frac{\left[ m_i^r(\lambda_j) - m_i^b(\lambda_j) - 2.5 \log M_i - E_i R \left( \frac{\lambda_j}{1+z_l} \right) \right]^2}{\sigma_{ij}^{b,2} + \sigma_{ij}^{r,2}} \quad (1)$$

where  $j$  is the filter index, superscripts  $b$  and  $r$  refer to the blue and red images in each pair, respectively, and  $\sigma_{ij}$  is the magnitude measurement uncertainty. We use the central wavelength of each

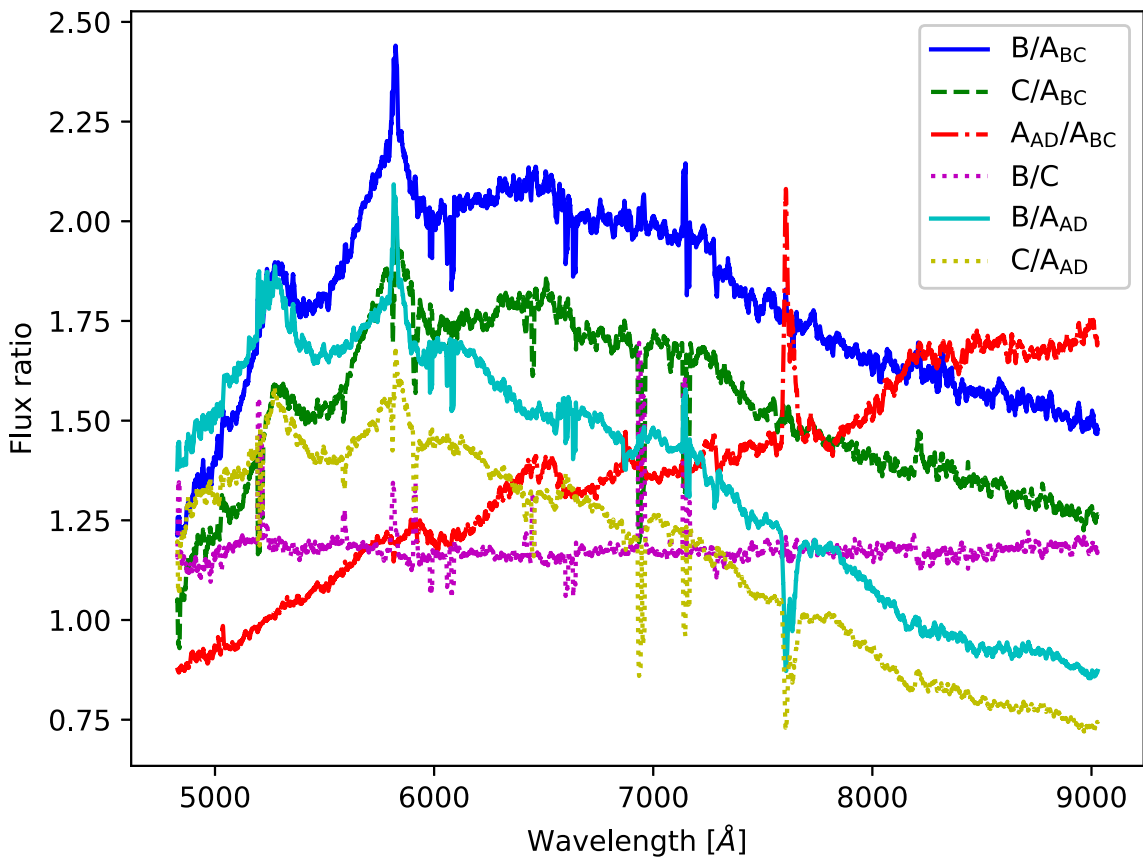


**Figure 7.** Measured spectral flux ratios in the region 4830–9030 Å, where the measurements are robust. The colours and line styles correspond to those in Fig. 6, except that some flux ratios have been inverted and photometric ratios involving image D have been replaced with spectroscopic ratios of  $A_{AD}$ . The spikes correspond to the intrinsic or atmospheric absorption lines in the original spectra.

filter, and the Cardelli, Clayton & Mathis (1989) extinction function implemented in the code EXTINCTION.<sup>10</sup> We perform the minimization using the Nelder–Mead (Nelder & Mead 1965) method implemented in SCIPY (Oliphant 2007), starting from random positions in the parameter space and further exploring around the solution with EMCEE (Foreman-Mackey et al. 2013), to ensure that we have found the global solution.

We find the best-fitting solution ( $\chi^2/d.o.f. = 213.4/16$ )<sup>11</sup> with  $z_l \sim 0.45$ ,  $R \sim 2.5$  slightly smaller than the Galactic extinction curve with  $R_V = 3.1$ , small  $E_i \lesssim 0.1$  consistent with the results in Falco et al. (1999), and flux ratios  $B/A = 1.28$ ,  $C/A = 1.20$ ,  $D/A = 0.30$ . These parameter values are robust if we remove from the fit all image pairs containing D (new fit  $\chi^2/d.o.f. = 145.8/10$ ), in case our decomposition of G and D is problematic due to the low image resolution. They are also robust to the choice of the extinction function. Except for  $B/C$ , which matches the prediction of the mass models, the flux ratios are smaller than predicted. The quality of the fits is statistically poor, although such large  $\chi^2$  values are found by Falco et al. (1999) in other lensing systems as well. In our analysis, we have ignored any contribution from microlensing and quasar

intrinsic variability, which can also affect flux ratios chromatically (e.g. Yonehara et al. 2008).

We can look for signs of microlensing by plotting the quasar image spectral ratios. While the overall shape of these ratios is sensitive to observational effects such as suboptimal slit placement and differential refraction, these (as well as differential extinction) should affect both continua and emission lines equally. On the other hand, microlensing is dependent on the size of the source, such that the continuum emission, which originates from a more compact region than the broad emission lines, should be preferentially microlensed. Fig. 7 clearly shows that, when dividing the fluxes of B and C to those of  $A_{BC}$  (i.e. the A+D+G signal, dominated by A, and extracted from the BC slit) and of  $A_{AD}$ , there is a large jump in the flux ratios at the locations of the SiIV/OIV] ( $\sim 5270\text{Å}$ ) and CIV ( $\sim 5800\text{Å}$ ) broad-line regions, compared to the surrounding continuum. On the other hand,  $B/C$  is relatively flat over the entire plotted range, which means that microlensing affects image A+D (the saddle points of the time arrival surface) but not B and C. A direct comparison of the photometric flux ratios in Fig. 6 with the spectroscopic ratios in Fig. 7 is not possible due to the fact that the spectra are affected by slit losses. Indeed, this can be seen from the monotonic variation in  $A_{AD}/A_{BC}$ , which we attribute to the fact that ESI does not use an atmospheric dispersion corrector, thus resulting in flux losses from differential refraction, particularly between the orthogonally placed AD and BC slits. Also, the data sets are not concurrent, and are therefore prone to time-varying microlensing and intrinsic variability effects.

<sup>10</sup><http://extinction.readthedocs.io/en/latest/>.

<sup>11</sup>With four images, thus three independent flux ratios in each band, and with eight bands, we have 24 constraints. As parameters, we have the redshift, the extinction curve parameter, three independent extinctions and 3 independent magnifications, thus eight parameters, resulting in 16 degrees of freedom.

As discussed above, microlensing in particular may affect the inferred lens redshift. We note that due to the low image resolution, proximity to image D, and morphological compactness which may affect the extracted photometry, we could not obtain a robust photometric redshift for this galaxy. Looser but more robust redshift constraints can be set by using the observed image separation and the estimated magnitude of the lens in the filter in which it is brightest. On the one hand, the image separation gives the lens velocity dispersion as a function of redshift; on the other, assuming an early-type spectral template, the measured magnitude can be converted into a rest-frame absolute magnitude as a function of redshift,<sup>12</sup> and then into a velocity dispersion (Faber & Jackson 1976). We find a lower limit of  $z_l \sim 0.5$ , below which the two velocity dispersion estimates disagree, and an upper limit of  $z_l \sim 1.5$ , above which the lens velocity dispersion is  $\sim 400 \text{ km s}^{-1}$ , a value above which the galaxy velocity dispersion function is vanishingly small (Sheth et al. 2003). The lower limit is close to the value inferred from our flux ratio analysis, and the upper one is consistent with the redshift of the narrow absorption systems identified in Section 4; it is also above the L18 estimate of  $z_l \sim 1$ .

## 6 CONCLUSIONS AND FUTURE WORK

We have carried out a systematic search for gravitationally lensed quasars in PS1, based on visual examination of cut-outs around the AGN source catalogue of Secrest et al. (2015), and aided by astrometric quantities measured by *Gaia*. We present our sample of 91 promising candidates, not found in the available literature, in Table 1, in order to enable follow-up observations by the interested community. We expect that the main source of contaminants are quasar pairs, which we see as a byproduct of our work, and to a lesser extent, quasar + star pairs. Our best estimate of the purity of our sample, in terms of lensed doubles and quasar pairs contaminated by quasar + star pairs, is  $\sim 70$  per cent.

As part of our search, we have independently discovered six known quads, including 2M113–2103. We present, for the first time, spectroscopy of this system, confirming it as a lensed quasar with source redshift  $z \sim 2.77$ . We identify absorption systems at  $z \sim 1.5$ , in three of the resolved quasar images, but we find these to be too narrow to attribute to the lensing galaxy. The image flux ratios show a monotonic dependence on wavelength, which we use to obtain a rough estimate of the lens redshift, under the assumption that the dependence is caused by extinction. The spectral flux ratios show evidence of microlensing in the combined emission from images A and D.

Our mass modelling confirms that 2M1134–2103 is affected by large shear, for which we identify two potential sources: a group of galaxies at  $z \sim 0.7$ , 30 arcsec from the lens, and another faint companion  $\sim 4$  arcsec away. Future multi-object spectroscopy is required to determine whether these are part of a larger cluster, or physically associated with the lens. The large image separation, brightness, and estimated time delays ranging from several days to several months, depending on the lens redshift, make this a valuable system to use for cosmography (e.g. Bonvin et al. 2017), provided that the environment can be characterized with future, deep imaging and spectroscopy (e.g. Wilson et al. 2016; Rusu et al. 2017; Sluse et al. 2017). High-resolution *Hubble Space Telescope* or adaptive optics imaging is necessary to constrain the morphology of the

lensing galaxy, and to further constrain the mass models using the expected extended emission from the underlying host galaxy (e.g. Chen et al. 2016; Wong et al. 2017).

## ACKNOWLEDGEMENTS

The authors are indebted to the anonymous referee for thoroughly checking the sample of candidates, resulting in a significant improvement of our selection, and for suggesting the use of *Gaia*. We also wish to thank Paul L. Schechter for his ‘matchmaking’ which has made this paper possible. This research made use of ASTROPY, a community-developed core PYTHON package for Astronomy (Astropy Collaboration 2013). Plots were produced with MATPLOTLIB (Hunter 2007). This work was supported by World Premier International Research Center Initiative (WPI Initiative), MEXT, Japan. CDF acknowledges support from the National Science Foundation under Grant No. AST-1715611.

The Pan-STARRS1 Surveys (PS1) and the PS1 public science archive have been made possible through contributions by the Institute for Astronomy, the University of Hawaii, the Pan-STARRS Project Office, the Max-Planck Society and its participating institutes, the Max Planck Institute for Astronomy, Heidelberg and the Max Planck Institute for Extraterrestrial Physics, Garching, The Johns Hopkins University, Durham University, the University of Edinburgh, the Queen’s University Belfast, the Harvard-Smithsonian Center for Astrophysics, the Las Cumbres Observatory Global Telescope Network Incorporated, the National Central University of Taiwan, the Space Telescope Science Institute, the National Aeronautics and Space Administration under Grant No. NNX08AR22G issued through the Planetary Science Division of the NASA Science Mission Directorate, the National Science Foundation Grant No. AST-1238877, the University of Maryland, Eotvos Lorand University (ELTE), the Los Alamos National Laboratory, and the Gordon and Betty Moore Foundation.

This work has made use of data from the European Space Agency (ESA) mission *Gaia* (<https://www.cosmos.esa.int/gaia>), processed by the *Gaia* Data Processing and Analysis Consortium (DPAC, <https://www.cosmos.esa.int/web/gaia/dpac/consortium>). Funding for the DPAC has been provided by national institutions, in particular the institutions participating in the *Gaia* Multilateral Agreement.

Based on observations obtained as part of the Visible and Infrared Survey Telescope for Astronomy (VISTA) Hemisphere Survey, ESO Program, 179.A–2010 (PI: McMahon). Based on data obtained from the ESO Science Archive Facility under request number cerusu312487.

Some of the data presented herein were obtained at the W. M. Keck Observatory, which is operated as a scientific partnership among the California Institute of Technology, the University of California and the National Aeronautics and Space Administration. The Observatory was made possible by the generous financial support of the W. M. Keck Foundation.

The authors recognize and acknowledge the very significant cultural role and reverence that the summit of Mauna Kea has always had within the indigenous Hawaiian community. We are most fortunate to have the opportunity to conduct observations from this superb mountain.

## REFERENCES

- Abolfathi B. et al., 2018, *ApJS*, 235, 42
- Agnello A., Spiniello C., 2018, preprint ([arXiv:1805.11103](https://arxiv.org/abs/1805.11103))
- Agnello A., Kelly B. C., Treu T., Marshall P. J., 2015, *MNRAS*, 448, 1446

<sup>12</sup>We use the MAG2MAG routine from Auger et al. (2009), available at <https://github.com/tcollett/LensPop/tree/master/stellarpop/>.

- Agnello A., Grillo C., Jones T., Treu T., Bonamigo M., Suyu S. H., 2018a, *MNRAS*, 474, 3391
- Agnello A. et al., 2018b, *MNRAS*, 475, 2086
- Agnello A. et al., 2018c, *MNRAS*, 479, 4345
- Aihara H. et al., 2018, *PASJ*, 70, S8
- Arenou F. et al., 2018, *A&A*, 616, A17
- Astropy Collaboration, 2013, *A&A*, 558, A33
- Auger M. W., Treu T., Bolton A. S., Gavazzi R., Koopmans L. V. E., Marshall P. J., Bundy K., Moustakas L. A., 2009, *ApJ*, 705, 1099
- Benítez N., 2000, *ApJ*, 536, 571
- Berghea C. T., Nelson G. J., Rusu C. E., Keeton C. R., Dudik R. P., 2017, *ApJ*, 844, 90
- Berlind A. A. et al., 2006, *ApJS*, 167, 1
- Bertin E., 2006, in Gabriel C., Arviset C., Ponz D., Solano E., eds, ASP Conf. Ser. Vol. 351, Astronomical Data Analysis Software and Systems XV. Astron. Soc. Pac., San Francisco, p. 112
- Bertin E., Arnouts S., 1996, *A&AS*, 117, 393
- Bertin E., Mellier Y., Radovich M., Missonnier G., Didelon P., Morin B., 2002, in Bohlender D. A., Durand D., Handley T. H., eds, ASP Conf. Ser. Vol. 281, Astronomical Data Analysis Software and Systems XI. Astron. Soc. Pac., San Francisco, p. 228
- Bettotti D., Falomo R., Scarpa R., Negrello M., Omizzolo A., Corradi R. L. M., Reverte D., Vulcani B., 2019, *ApJ*, 873, L14
- Bonvin V. et al., 2017, *MNRAS*, 465, 4914
- Cardelli J. A., Clayton G. C., Mathis J. S., 1989, *ApJ*, 345, 245
- Chambers K. C. et al., 2016, (PS1) preprint ([arXiv:1612.05560](https://arxiv.org/abs/1612.05560))
- Chan J. H. H., Suyu S. H., Chiueh T., More A., Marshall P. J., Coupon J., Oguri M., Price P., 2015, *ApJ*, 807, 138
- Chen G. C.-F. et al., 2016, *MNRAS*, 462, 3457
- Claeskens J.-F., Surdej J., 2002, *A&AR*, 10, 263
- Colless M. et al., 2001, *MNRAS*, 328, 1039
- Croom S. M., Smith R. J., Boyle B. J., Shanks T., Loaring N. S., Miller L., Lewis I. J., 2001, *MNRAS*, 322, L29
- D'Abrusco R., Massaro F., Paggi A., Smith H. A., Masetti N., Landoni M., Tosti G., 2014, *ApJS*, 215, 14
- da Cunha E. et al., 2017, *Publ. Astron. Soc. Aust.*, 34, e047
- Delchambre L. et al., 2019, *A&A*, 622, A165
- de Vaucouleurs G., 1948, *Ann. Astrophys.*, 11, 247
- Faber S. M., Jackson R. E., 1976, *ApJ*, 204, 668
- Fabricius C. et al., 2016, *A&A*, 595, A3
- Falco E. E. et al., 1999, *ApJ*, 523, 617
- Findlay J. R. et al., 2018, *ApJS*, 236, 44
- Flauger B. et al., 2015, *AJ*, 150, 150
- Flesch E. W., 2015, *Publ. Astron. Soc. Aust.*, 32, e010
- Flewelling H. A. et al., 2016, preprint ([arXiv:1612.05243](https://arxiv.org/abs/1612.05243))
- Foreman-Mackey D., Hogg D. W., Lang D., Goodman J., 2013, *PASP*, 125, 306
- Gaia Collaboration, 2016, *A&A*, 595, A1
- Gaia Collaboration, 2018a, *A&A*, 616, A1
- Gaia Collaboration, 2018b, *A&A*, 616, A14
- Healey S. E. et al., 2008, *ApJS*, 175, 97
- Hennawi J. F. et al., 2006, *AJ*, 131, 1
- Hennawi J. F. et al., 2010, *ApJ*, 719, 1672
- Henstock D. R., Browne I. W. A., Wilkinson P. N., McMahon R. G., 1997, *MNRAS*, 290, 380
- Holder G. P., Schechter P. L., 2003, *ApJ*, 589, 688
- Hopkins P. F., Hernquist L., Cox T. J., Di Matteo T., Robertson B., Springel V., 2006, *ApJS*, 163, 1
- Hopkins P. F., Hernquist L., Cox T. J., Kereš D., 2008, *ApJS*, 175, 356
- Hunter J. D., 2007, *Comput. Sci. Eng.*, 9, 90
- Huo Z.-Y. et al., 2013, *AJ*, 145, 159
- Inada N. et al., 2003, *Nature*, 426, 810
- Inada N. et al., 2008, *AJ*, 135, 496
- Inada N. et al., 2010, *AJ*, 140, 403
- Inada N. et al., 2012, *AJ*, 143, 119
- Inada N., Oguri M., Rusu C. E., Kayo I., Morokuma T., 2014, *AJ*, 147, 153
- Jackson N., Rampadarath H., Ofek E. O., Oguri M., Shin M.-S., 2012, *MNRAS*, 419, 2014
- Jean C., Surdej J., 1998, *A&A*, 339, 729
- Jones D. H. et al., 2009, *MNRAS*, 399, 683
- Kayo I., Oguri M., 2012, *MNRAS*, 424, 1363
- Kayo I., Inada N., Oguri M., Morokuma T., Hall P. B., Kochanek C. S., Schneider D. P., 2010, *AJ*, 139, 1614
- Keeton C. R., Kochanek C. S., Falco E. E., 1998, *ApJ*, 509, 561
- Kleinman S. J. et al., 2013, *ApJS*, 204, 5
- Kneib J.-P., Cohen J. G., Hjorth J., 2000, *ApJ*, 544, L35
- Koposov S. E., Belokurov V., Torrealba G., 2017, *MNRAS*, 470, 2702
- Kostrzewa-Rutkowska Z. et al., 2018, *MNRAS*, 476, 663
- Lee C.-H., 2018, *MNRAS*, 475, 3086
- Lemon C. A., Auger M. W., McMahon R. G., Koposov S. E., 2017, *MNRAS*, 472, 5023
- Lemon C. A., Auger M. W., McMahon R. G., Ostrovski F., 2018, *MNRAS*, 479, 5060
- Lemon C. A., Auger M. W., McMahon R. G., 2019, *MNRAS*, 483, 4242
- Lucey J. R., Schechter P. L., Smith R. J., Anguita T., 2018, *MNRAS*, 476, 927 (L18)
- Maddox S. J., Sutherland W. J., Efstathiou G., Loveday J., 1990, *MNRAS*, 243, 692
- Magain P., Letawe G., Courbin F., Jablonka P., Jahnke K., Meylan G., Wisotzki L., 2005, *Nature*, 437, 381
- Magnier E. A. et al., 2016a, preprint ([arXiv:1612.05240](https://arxiv.org/abs/1612.05240))
- Magnier E. A. et al., 2016b, preprint ([arXiv:1612.05242](https://arxiv.org/abs/1612.05242))
- McMahon R. G., Banerji M., Gonzalez E., Koposov S. E., Bejar V. J., Lodieu N., Rebolo R., VHS Collaboration, 2013, *Messenger*, 154, 35 (VHS)
- Moffat A. F. J., 1969, *A&A*, 3, 455
- More A. et al., 2016, *MNRAS*, 456, 1595
- Nelder J. A., Mead R., 1965, *Comput. J.*, 7, 308
- Ochner P. et al., 2014, *Astron. Telegram*, 6750,, 1
- Ofek E. O., Oguri M., Jackson N., Inada N., Kayo I., 2007, *MNRAS*, 382, 412
- Oguri M., 2010, *PASJ*, 62, 1017
- Oguri M., Marshall P. J., 2010, *MNRAS*, 405, 2579
- Oguri M. et al., 2005, *ApJ*, 622, 106
- Oguri M. et al., 2006, *AJ*, 132, 999
- Oguri M. et al., 2012, *AJ*, 143, 120
- Oiphant T. E., 2007, *Comput. Sci. Eng.*, 9, 10
- Onaka P., Tonry J. L., Isani S., Lee A., Uyeshiro R., Rae C., Robertson L., Ching G., 2008, in McLean I. S., Casali M. M., eds, Proc. SPIE Conf. Ser. Vol. 7014, Ground-based and Airborne Instrumentation for Astronomy II. SPIE, Bellingham, p. 70140D
- Ostrovski F. et al., 2017, *MNRAS*, 465, 4325
- Ostrovski F. et al., 2018, *MNRAS*, 473, L116
- Peng C. Y. et al., 1999, *ApJ*, 524, 572
- Rusu C. E., Lemon C. A., 2018, *Res. Notes Am. Astron. Soc.*, 2, 187
- Rusu C. E., Oguri M., Iye M., Inada N., Kayo I., Shin M.-S., Sluse D., Strauss M. A., 2013, *ApJ*, 765, 139
- Rusu C. E. et al., 2016, *MNRAS*, 458, 2
- Rusu C. E. et al., 2017, *MNRAS*, 467, 4220
- Sergeyev A. V., Zheleznyak A. P., Shalyapin V. N., Goicoechea L. J., 2016, *MNRAS*, 456, 1948
- Schechter P. L., Pooley D., Blackburne J. A., Wambsganss J., 2014, *ApJ*, 793, 96
- Schlafly E. F., Finkbeiner D. P., 2011, *ApJ*, 737, 103
- Secrest N. J., Dudik R. P., Dorland B. N., Zacharias N., Makarov V., Fey A., Frouard J., Finch C., 2015, *ApJS*, 221, 12
- Shanks T. et al., 2015, *MNRAS*, 451, 4238
- Scheinis A. I., Bolte M., Epps H. W., Kibrick R. I., Miller J. S., Radovan M. V., Bigelow B. C., Sutin B. M., 2002, *PASP*, 114, 851
- Sheth R. K. et al., 2003, *ApJ*, 594, 225
- Skrutskie M. F. et al., 1997, *The Impact of Large Scale Near-IR Sky Surveys*, Kluwer, Dordrecht, p. 25
- Sluse D., Chantry V., Magain P., Courbin F., Meylan G., 2012, *A&A*, 538, A99
- Sluse D. et al., 2017, *MNRAS*, 470, 4838
- Spinelli C. et al., 2018, *MNRAS*, 480, 1163
- Surdej J. et al., 1987, *Nature*, 329, 695

- Szabo T., Pierpaoli E., Dong F., Pipino A., Gunn J., 2011, *ApJ*, 736, 21  
 Taylor M. B., 2005, in Shopbell P., Britton M., Ebert R., eds, ASP Conf. Ser. Vol. 347, Astronomical Data Analysis Software and Systems XIV. Astron. Soc. Pac., San Francisco, p. 29  
 Tonry J., Onaka P., 2009, in Ryan S., ed., Proceedings of the Advanced Maui Optical and Space Surveillance Technologies Conference. The Maui Economic Development Board, Kihei, HI, p. E40  
 Treu T., Marshall P. J., 2016, *A&AR*, 24, 11  
 Weymann R. J., Latham D., Angel J. R. P., Green R. F., Liebert J. W., Turnshek D. A., Turnshek D. E., Tyson J. A., 1980, *Nature*, 285, 641  
 Williams P., Agnello A., Treu T., 2017, *MNRAS*, 466, 3088  
 Wilson M. L., Zabludoff A. I., Ammons S. M., Momcheva I. G., Williams K. A., Keeton C. R., 2016, *ApJ*, 833, 194  
 Wisotzki L., Koehler T., Kayser R., Reimers D., 1993, *A&A*, 278, L15  
 Wong K. C. et al., 2017, *MNRAS*, 465, 4895  
 Wright E. L. et al., 2010, *AJ*, 140, 1868  
 Yonehara A., Hirashita H., Richter P., 2008, *A&A*, 478, 95  
 York D. G. et al., 2000, *AJ*, 120, 1579

## APPENDIX A: EXPECTED SAMPLE PURITY FROM THE RELATIVE DENSITY OF GAIA AND AGN SOURCES

We start with the complete *Gaia* DR2 source catalogue,<sup>13</sup> where we apply the same automatic selection cuts we used for our sample of candidates. We use a bright magnitude limit of  $G \geq 17.5$ , slightly brighter than our candidate source companions, and a faint one of  $G \leq 20$ . While 29 of the 91 candidate source companions are fainter than  $G = 20$ , we apply this cut because *Gaia* DR2 is still

complete at this limit (Arenou et al. 2018), outside the crowded regions excluded by our galactic latitude cut; the completeness is expected to drop towards the limiting magnitude of  $G \sim 21$ . This reduces the *Gaia* catalogue to  $\sim 148$  million sources. We also apply a colour cut of  $0 \leq Rp - Bp \leq 1.5$ , from Fig. 1, as well as the same *Gaia*-based astrometric quantity cuts from Section 2.2. As we did for our candidates, we keep the objects without *Gaia* astrometric quantities or colour. This results in  $\sim 22$  million remaining sources.

The Secrest et al. (2015) AGN catalogue is less complete, but not significantly so, with a limiting magnitude of 20 in *g* band, or about the same in *Gaia G* band.<sup>14</sup> We use the Milliquas catalogue (Flesch 2015), which is slightly more complete at this magnitude limit (see fig. 3 in Lemon et al. 2019), and includes high-confidence quasars detected in X-ray and radio, in addition to *WISE*. We cross-matched the *Gaia* catalogue after performing the cuts described above with the Milliquas catalogue, resulting in  $\sim 520\,000$  matches.

Finally, the *Gaia* resolution is much higher than the one of *WISE*, with PSF FWHM  $\sim 6$  arcsec (Wright et al. 2010). We use TOPCAT (Taylor 2005) to identify all objects from the *Gaia*-based catalogue we produced above with relative separation less than the *WISE* PSF FWHM, and count each of these clusters as one. This reduces the *Gaia*-based sample to  $\sim 14$  million sources, resulting in an AGN fraction of  $\sim 4$  per cent.

## APPENDIX B: PREVIOUSLY CONFIRMED OR RULED OUT CANDIDATES

<sup>13</sup><https://www.astro.rug.nl/gaia/>.

<sup>14</sup>From our 312 candidates,  $G - g$  has a distribution with a median of  $-0.21$  and a standard deviation of 0.34

**Table B1.** Previously confirmed candidates, and those ruled out by *Gaia* data or existing spectroscopy.

Name (PS1 J...)	$\alpha$	$\delta$	#Comp	$i$	Sep. (arcsec)	Rank	Notes
013459+243049	23.745589	24.513635	2	19.40	3.7	C	$G = 19.60, 20.17; p-l$ ; two SDSS QSOs at $z = 2.093$ and $z = 2.104$
014710+463043	26.792452	46.512081	2	15.57	3.2	A	$G = 15.89, 16.18, 16.74, 18.26$ ; similar colour p-l sources; PSJ0147+4630 (quad; Berghea et al. 2017)
024526–055700	41.356685	–5.950128	2	18.67	1.7	C	$G = 19.73, 19.25$ ; similar colour p-l + red inner component; DESJ0245–0556 (double; Agnello et al. 2018b)
025934–233802	44.889982	–23.633792	2	19.21	2.7	B	$G = 20.34, 19.37; p-l + red inner component$ ; PSJ0259–2338 (double; Lemon et al. 2018)
094235+231030	145.645825	23.175133	2	18.87	2.4	C	$G = 19.10, 19.92$ ; similar colour p-l; $z = 1.83$ QSO pair (Findlay et al. 2018)
110633–182124	166.639282	–18.356688	2	16.95	3.1	C	$G = 17.07, 18.20$ ; similar colour p-l; HE1104–1805 (double; Wisotzki et al. 1993)
110932+531636	167.384487	53.276552	2	18.71	3.2	C	$G = 18.97, 19.68$ ; similar colour p-l; includes SDSS $z = 0.982$ QSO; SQLS QSO pair
113441–210323	173.668953	–21.056307	3	16.81	3.7	A	$G = 17.17, 17.19, 18.94, 17.27$ ; four p-l sources; 2M1134–2103 (quad; Lucey et al. 2018)
120451+442836	181.210712	44.47659	2	18.84	3.0	B	$G = 18.81, 19.65$ ; similar colour p-l; SQLS QSO at $z = 1.84$ and $z = 1.14$
120630+433219	181.623684	43.538734	2	18.52	3.0	B	$G = 18.87, 18.84$ ; similar colour p-l + red component; SDSSJ1206+4332 (double; Oguri et al. 2005)
120659–254331	181.744763	–25.725376	2	19.41	2.1	B	$G = 19.97, 20.40$ ; similar colour p-l; both have negligible AEN, pm, and p; double, discovered, and confirmed independently by C. Lemon, private communication
124614+503049	191.556942	50.513634	2	19.22	2.4	C	$G = 19.31, 19.50$ ; similar colour p-l; SDSS quasar pair $z = 2.73, 2.11$
132100+164403	200.246658	16.734072	3	18.51	8.8	B	$G = 18.66, 19.46$ ; similar colour p-l + red component; SDSSJ1320+1644 (double or binary quasar; Rusu et al. 2013)
133713+601208	204.304581	60.202141	2	18.55	3.1	C	$G = 18.68, 19.63$ ; similar colour p-l; $z = 1.721, 1.726$ QSO pair (Hennawi et al. 2006)
140515+095930	211.314397	9.991796	2	18.96	1.9	B	$G = 19.38, 20.32$ ; p-l + extended red; ULAS J1405+0959 (double; Jackson et al. 2012)
141818–161008	214.573673	–16.168771	2	18.53	2.4	C	$G = 18.46, 19.33$ ; similar colour p-l; NIQ $z = 1.13$ (Lemon et al. 2019)
143323+600715	218.345158	60.120864	5	19.49	3.7	A	$G = 19.87, 19.99, 20.26$ ; p-l; SDSSJ1433+6007 (quad; Agnello et al. 2018a)
143351+145007	218.462505	14.835308	2	18.90	3.3	C	$G = 18.99, 19.35$ ; similar colour p-l; $z = 1.51$ QSO pair (Findlay et al. 2018)
151539+151135	228.910562	15.193168	2	17.94	2.0	C	$G = 18.03, 18.42$ ; similar colour p-l; SDSSJ1515+1511 (double; I마다 et al. 2014)
153725–301017	234.355599	–30.171336	4	19.12	3.1	A	$G = 20.32, 20.22, 20.44$ ; four p-l + inner red component; (quad; Delchambre et al. 2019; Lemon et al. 2019)
160600–233322	241.500981	–23.556046	3	17.96	2.9	C	$G = 18.85, 18.97, 19.33, 19.61$ ; p-l + red component; PSJ1606–2333 (quad; Lemon et al. 2018)
172145+884222	260.43637	88.706169	2	17.33	2.3	B	$G = 18.18, 18.33$ ; similar colour; PSJ1721+8842 (quad; Lemon et al. 2018)
203238–235822	308.157206	–23.972856	2	18.75	2.0	C	$G = 19.12, 19.26$ ; similar colour p-l; $z = 1.64$ NIQ (Lemon et al. 2018)
215316+273235	328.31765	27.543058	2	18.69	3.6	C	$G = 18.72, 19.69$ ; similar colour p-ls; quasar pair (Sergeyev et al. 2016)
221208+314417	333.033412	31.73809	2	19.27	2.6	C	$G = 19.28, 19.97$ ; two similar colour p-l + red component; (double; Lemon et al. 2019)
000823+031342	2.094362	3.228219	2	17.70	3.2	C	p-l; PB 5757 (star), large pm
001313–152007	3.302628	–15.335383	2	16.82	1.9	C	similar colour p-l; companion has large pm
002605+401519	6.5222825	40.255255	2	17.85	2.3	C	p-l; companion has large pm
002719+300336	6.827338	30.059894	2	17.90	3.0	C	similar colour p-l; companion has large pm
004346+282715	10.942056	28.454297	2	17.58	3.3	C	point sources; bright component has large pm and p
004446+472400	11.192613	47.399741	2	18.13	3.3	C	similar colour p-l; companion has large pm
005801–231711	14.502676	–23.286411	2	17.82	3.1	C	similar colour p-l; one component has large pm
011305+454905	18.26259	45.818058	2	17.60	1.7	C	similar colour p-l; companion has large pm
011639+405252	19.163546	40.881125	2	18.72	1.3	C	similar colour p-l; includes SDSS $z = 1.86$ QSO; one component has large pm
015109+315521	27.78604	31.922389	2	18.11	3.1	C	includes galaxy (Ochner et al. 2014); companion has large pm
020122+212637	30.340775	21.443685	2	17.45	3.6	C	similar colour p-l; SQLS candidate; companion has large pm
020649+803347	31.703677	80.563065	2	17.36	2.2	C	similar colour p-l; companion has large pm and p
020722+374720	31.843188	37.788868	2	16.60	2.2	C	similar colour p-l +extended; companion has large pm and p

Table B1 – continued

Name (PS1 J..)	$\alpha$	$\delta$	#Comp	$i$	Sep. (arcsec)	Rank	Notes
024414–073747	41.059791	–7.629853	2	19.75	1.4	C	p-l; includes $z = 0.319$ galaxy (Szabo et al. 2011); companion has no <i>Gaia</i> pm and p
024722–172547	41.843352	–17.429683	2	18.67	1.6	C	similar colour p-l; companion has large pm
025339+070440	43.414166	7.077896	2	18.17	2.8	C	similar colour p-l; companion has large pm
025644+394153	44.183373	39.697932	2	19.28	2.4	C	similar colour p-l; companion has large pm
034955–071723	57.479613	–7.289607	2	16.12	2.5	C	p-l; companion has large pm and p
035119–182302	57.829409	–18.383904	2	16.92	1.8	C	p-l; companion has large pm and p
041304+1526106	63.266175	15.868444	2	17.60	3.5	C	similar colour p-l; companion has large pm
043324–111537	68.348462	–11.260161	2	18.31	2.7	C	similar colour p-l; companion has large pm
045230–295335	73.125436	–29.893138	2	15.36	2.0	B	similar colour p-l + extended? star + interacting galaxy + QSO HE0450–2958 (Magain et al. 2005)
051139–035102	77.911071	–3.850553	2	19.02	2.9	C	similar colour p-l; QSO + other (Lemon et al. 2018); both negligible AEN, pm, and p
052131+730136	80.380313	73.026614	2	17.55	3.0	C	p-l; companion has large pm and p
052419–065727	81.077162	–6.957592	2	16.98	1.8	C	p-l; companion has large pm
052833+042744	82.136604	4.462234	2	16.72	1.9	C	p-l; companion has large pm
053733+815634	84.386019	81.942802	2	18.72	3.2	C	similar colour p-l; companion has large pm
054335–152624	85.894214	–15.439864	2	17.63	2.8	C	p-l; companion has large pm
061050–201839	92.710135	–20.310915	2	18.37	2.8	C	different colour p-l; outer component has large pm
061911–295857	94.796622	–29.982405	3	18.70	2.3	C	p-l; companion has large pm
062529–285546	96.371981	–28.929452	2	18.25	3.0	C	(2019) <i>Gaia</i> clusters catalogue
063724+434603	99.34909	43.767531	3	16.9	5.3	C	p-l; companion has large pm
065513+850519	103.804667	85.088737	3	17.50	4.5	B	similar colour p-l (companion has large pm) + red inner component (large AEN); included in the Delchambre et al. (2019) <i>Gaia</i> clusters catalogue
072846+420701	112.190784	42.116988	2	16.79	3.9	C	similar colour p-l; includes SDSS $z = 1.120$ QSO; SQLS candidate; companion has large pm and p
072850+f70125	112.206878	57.02358	2	16.03	3.5	C	p-l; includes $z = 0.426$ Seyfert 1 (Henslock et al. 1997); companion has large pm and p
074244+651038	115.673761	65.177097	2	15.17	2.0	C	similar colour p-l (companion has large pm) + red inner component (large AEN); included in the Delchambre et al. (2019) <i>Gaia</i> clusters catalogue
074555+181818	116.478082	18.304882	2	17.80	2.5	C	consistent with single extended source; Mrk 78 (Seyfert 2); no <i>Gaia</i> data
080938+275648	122.407538	27.946714	2	17.09	3.1	C	p-l; includes SDSS $z = 1.060$ QSO; SQLS candidate; companion has large pm
081130+255541	122.876253	25.927955	2	18.96	2.7	C	similar colour p-l; includes SDSS $z = 0.406$ QSO; companion has large pm and p
082218+665957	125.574156	66.999183	2	18.61	3.0	C	p-l; companion has large pm
082353–085114	125.970487	–8.853931	2	16.88	2.2	C	similar colour p-l; companion has large pm and p
082442+592409	126.176996	59.402484	2	17.77	3.1	C	similar colour p-l; companion has large pm
083229+563235	128.119012	56.542997	3	18.76	3.0	C	similar colour p-l (companion has large pm) + inner red component; includes SDSS $z = 0.683$ QSO; SQLS QSO + star
084441+334909	131.16938	33.819226	2	18.28	2.9	C	similar colour p-l; includes SDSS $z = 1.425$ QSO; SQLS candidate; companion has large pm
084513+543422	131.302961	54.57264	2	18.51	1.4	C	similar colour p-l; includes SDSS $z = 1.290$ QSO; SQLS QSO + star (large pm)
085055–052735	132.72728	–5.459747	2	19.11	2.0	C	similar colour p-l; companion has large pm
085838–152907	134.656619	–15.485172	2	17.27	2.5	C	similar colour p-l; companion has large pm
090852+304332	137.215844	30.725594	2	18.51	2.1	C	p-l; includes SDSS $z = 0.399$ Seyfert 1; companion has large pm
091455–265223	138.722422	–26.873106	2	17.80	2.4	C	similar colour p-l; companion has large pm
091746–160623	139.443706	–16.106479	4	18.41	2.3	C	similar colour p-l; companion has large pm; included in the Delchambre et al. (2019) <i>Gaia</i> clusters catalogue
092016–063144	140.064718	–6.529	2	18.16	2.7	C	similar colour p-l; companion has large pm
092438–012845	141.157105	–1.479089	2	17.99	3.0	C	similar colour p-l; includes SDSS $z = 2.446$ QSO; companion has large pm

**Table B1 – continued**

Name (PS1 J...)	$\alpha$	$\delta$	#Comp	$i$	Sep. (arcsec)	Rank	Notes
092718+211357	141.826656	21.232549	2	17.47	2.3	C	p-l; includes SDSS $z = 1.851$ QSO; SQLS candidate, no lensing object; companion has large pm
094115+305810	145.314113	30.969479	2	19.29	2.3	C	similar colour; SQLS $z = 1.193$ QSO + blue galaxy
094437+263355	146.154045	-26.365394	2	16.77	2.3	C	similar colour; includes Seyfert 1 galaxy at $z = 0.142$ (Jones et al. 2009) companion has large pm
094903+280022	147.264552	28.006127	2	18.79	1.2	C	similar colour p-l; SQLS QSO + star
100450+773753	151.208619	77.63132	2	19.05	1.9	C	similar colour p-l; companion has large pm
102803+153028	157.011143	-15.507813	3	19.60	4.5	B	p-l + red inner component (large pm)
102813+171902	157.054777	17.317297	2	18.53	1.9	C	p-l; only one component has <i>Gaia</i> p and pm, large pm
104704+241459	161.763852	-24.249719	2	16.95	2.8	B	similar colour p-l (companion has large pm) + red inner component
105852+275715	164.715138	-27.954048	2	18.01	2.4	C	similar colour p-l; companion has large pm
111524+042218	168.848654	-4.371723	2	18.60	2.7	C	similar colour p-l; includes galaxy at $z = 0.209$ (Colless et al. 2001); no <i>Gaia</i> p and pm, large AEN for companion
113431+111918	173.628607	11.321701	2	18.49	1.6	C	similar colour p-l; large companion pm; $z = 1.62$ QSO + star (Ostrovski et al. in preparation)
114214-075619	175.556357	-7.938667	2	18.93	3.4	C	similar colour p-l; companion has large pm
115443-224432	178.680182	-22.742147	2	17.75	2.4	B	similar colour p-l; companion has large pm
115541+131105	178.919792	13.184774	2	17.52	2.4	B	similar colour p-l; companion has large pm
115957+644406	179.987136	64.735049	2	18.77	3.1	C	similar colour p-l; includes SDSS $z = 1.61$ QSO; companion has large pm
123441+341000	188.672008	34.166556	2	18.29	2.2	C	similar colour p-l; includes SDSS $z = 1.429$ QSO, SQLS candidate; companion has large pm
123559-023503	188.993809	-2.58423	2	17.78	3.0	C	similar colour p-l; SDSS $z = 2.062$ QSO + star, SQLS candidate
130738+640252	196.907012	64.047899	2	18.17	3.5	C	similar colour p-l; companion has large pm
131425+181232	198.605024	18.208753	2	19.46	2.5	C	p-l; companion has large pm
132225+512017	200.595155	51.338029	2	18.29	2.7	C	similar colour p-l; includes SDSS $z = 1.772$ QSO; SQLS candidate; companion has large pm
132405+282334	201.022027	28.392698	2	18.54	2.1	C	similar colour p-l; includes SDSS $z = 0.904$ QSO; SQLS candidate; no lensing object; companion has large pm
132853+261501	202.222599	26.250248	2	18.91	2.6	C	similar colour p-l; SQLS candidate; SDSS $z = 1.522$ QSO + star; companion has large pm
132916+414554	202.31656	41.765054	2	17.59	2.8	C	similar colour p-l; companion has large pm
133543-294239	203.927943	-29.710967	2	18.50	2.4	C	p-l; companion has large pm
134222-261001	205.593589	-26.166945	2	18.30	2.9	C	similar colour p-l; companion has large pm
134539-262819	206.411024	-26.471915	2	17.82	2.6	C	similar colour p-l; companion has large pm
134620+045245	206.609217	4.879294	2	18.73	2.7	C	similar colour p-l; companion has large pm
134944+011054	207.420114	1.181594	2	16.55	2.2	C	similar colour p-l; includes SDSS star
140610-250809	211.54001	-25.135907	2	17.88	2.9	B	similar colour p-l; companion has large pm
141340+475113	213.452222	47.853718	2	18.55	3.0	C	similar colour p-l; includes SDSS $z = 2.175$ QSO; SQLS candidate; no lensing object; companion has large pm
141432-052951	213.631386	-5.49754	2	19.17	2.2	C	similar colour p-l; companion has large pm
142040+122507	215.16569	12.418669	2	18.31	3.1	C	similar colour p-l; includes SDSS $z = 2.252$ QSO; companion has large pm
142402+710911	216.008966	71.152985	2	18.70	2.9	C	similar colour p-l; companion has large pm
142609-210327	216.538323	-21.057381	2	19.44	2.8	C	similar colour p-l; companion has large pm
143155-094341	217.972653	-9.727974	3	18.56	5.8	B	p-l (companion has large pm) + red inner component
143154+530033	217.975863	53.009266	3	18.09	4.3	C	p-l; includes SDSS $z = 1.389$ QSO + star; third component has large pm included in the Delchambre et al. (2019) <i>Gaia</i> clusters catalogue
143245-273713	218.188947	-27.620192	2	17.78	3.0	C	similar colour p-l; companion has large pm
144145+023743	220.437914	2.628697	2	19.13	1.1	C	similar colour p-l; SQLS $z = 1.160$ QSO + star
144245+041619	220.689582	4.271996	2	19.27	3.0	C	p-l; includes SDSS $z = 2.012$ QSO; SQLS candidate; companion has large pm

Table B1 – continued

Name (PS1 J...)	$\alpha$	$\delta$	#Comp	$i$	Sep. (arcsec)	Rank	Notes
144303+260329	220.763978	26.058137	2	17.98	3.5	C	similar colour p-l; includes SDSS $z = 0.257$ Seyfert 1; companion has large pm
145115+052936	222.813312	5.493197	2	16.20	2.3	C	similar colour p-l; includes SDSS $z = 2.052$ QSO; SQLS candidate; companion has large pm
145232-052947	223.134353	-5.496432	2	18.04	2.9	C	p-l + red inner component; companion has large pm
145647-091751	224.197573	-9.297562	2	17.99	3.0	C	similar colour p-l; companion has large p and pm
150925+113851	227.35556	11.647604	2	19.37	2.5	C	similar colour p-l; includes SDSS star; only one component has <i>Gaia</i> p and pm, negligible values
151044-074043	227.684808	-7.678621	2	18.27	2.5	C	similar colour p-l; companion has large pm
151205+182706	228.018788	18.451666	2	17.76	2.5	C	similar colour p-l; companion has large pm
151237+553901	228.15381	55.650295	2	19.01	1.9	C	similar colour p-l; includes SDSS $z = 1.363$ QSO; SQLS QSO + star
151527-203609	228.862483	-20.602366	2	17.84	2.9	C	p-l; companion has large pm
151832+343325	229.632917	34.557016	2	18.87	3.0	C	similar colour p-l; includes SDSS $z = 1.672$ QSO; SQLS candidate; companion has large pm
151858-022443	229.741319	-2.411924	3	16.9	3.3	B	p-l; inner component has large pm, the other two have negligible AEN, p and pm
151918+094205	229.826754	9.701277	2	18.11	3.7	C	similar colour p-l; companion has large pm
152005+195038	230.021454	19.843884	3	18.73	1.4	C	similar colour; a single companion has <i>Gaia</i> data (only AEN, large p-l; includes SDSS $z = 1.365$ QSO; SQLS candidate candidate; companion has large p and pm
152050+263741	230.209019	26.627994	2	18.93	2.1	C	similar colour p-l; includes SDSS $z = 1.445$ QSO; SQLS candidate; companion has large pm
152444+054628	231.182118	5.774438	2	17.68	3.7	C	similar colour p-l; companion has large pm
153223-291257	233.094482	-29.215933	2	19.05	1.8	C	similar colours; only one, outer component has <i>Gaia</i> data, large pm, the others are galaxies
153311-001509	233.296204	-0.252541	3	19.49	4.0	C	p-l; third component? includes SDSS $z = 1.953$ QSO; SQLS candidate; companion has large pm
153510+082347	233.790155	8.396438	2	18.77	2.5	C	similar colour p-l; companion has large pm
154226-023456	235.610402	-2.582135	2	18.74	3.1	C	similar colour p-l; companion has large pm
154726-153237	236.857051	-15.543614	2	17.96	2.7	C	similar colour p-l; companion has large pm
160138+172852	240.407737	17.48102	3	17.80	5.6	C	similar colour p-l (one component has large pm) + red inner components (large pm); includes SDSS $z = 2.239$ QSO
160922+175431	242.361547	17.90869	2	17.67	2.6	C	similar colour p-l; includes SDSS $z = 1.993$ QSO; SQLS candidate; companion has large pm
161008+234837	242.533565	23.810394	2	19.14	3.0	C	similar colour p-l; companion has large pm
161657-170647	244.233836	-17.113065	2	18.12	2.6	C	similar colour p-l; companion has large pm
161722-230546	244.340087	-23.096165	2	18.80	1.8	C	similar colour p-l; QSO + star (Lemon et al. 2018)
161841+301311	244.669946	30.2196	2	17.61	2.5	B	similar colour p-l; includes SDSS $z = 1.403$ QSO; companion has large pm
161931+162123	244.878602	16.356363	2	19.08	2.6	C	similar colour p-l; includes SDSS $z = 2.455$ QSO; companion has large pm
162417+064152	246.070533	6.697785	2	18.44	2.4	C	similar colour p-l; companion has large pm
163113-171407	247.804331	-17.235305	2	17.59	3.0	C	similar colour p-l; companion has large pm
163533+205229	248.886788	20.87476	2	18.49	2.1	C	similar colour p-l; companion has large pm
163614+094317	249.056552	9.721352	2	19.21	2.2	C	similar colour p-l; 2 components have large pm
163959-210652	249.995488	-21.114331	2	18.84	1.7	C	similar colour p-l; companion has large pm
164304+754120	250.763894	75.688987	2	18.08	3.5	C	similar colour p-l; companion has large pm
164552+152025	251.465796	15.340377	2	19.04	2.2	B	similar colour p-l; companion has large pm
170002+250336	255.009344	25.060094	3	18.50	4.7	C	similar colour p-l; 2 components have large pm
170024+005815	255.099997	0.970862	2	16.44	1.6	C	similar colour p-l; companion has large pm
170514+331327	256.307089	33.276899	2	18.98	2.2	C	similar colour p-l; includes SDSS $z = 2.224$ QSO; companion has large pm
170516+251533	256.310261	25.259123	2	18.34	2.1	C	similar colour p-l; companion has large pm
170602+220715	256.509411	27.087583	2	17.31	2.3	C	similar colour; one component has large pm, the other one large AEN

Table B1 – continued

Name (PS1 J...)	$\alpha$	$\delta$	#Comp	$i$	Sep. (arcsec)	Rank	Notes
170817+325311	257.072403	32.886393	2	18.38	2.1	C	similar colour p-l; companion has large AEN and pm
170858–030510	257.240718	–3.086224	2	17.60	2.5	C	p-l; companion has large pm
170943+334304	257.427474	33.717724	2	19.13	3.3	C	similar colour p-l; both have large pm
171102+292951	257.757094	29.497482	2	17.92	2.2	C	similar colour p-l; includes SDSS $z = 1.329$ QSO; SQLS candidate; companion has large pm; no lensing object
172634+530300	261.639624	53.050095	2	18.76	1.3	C	similar colour p-l; includes white dwarf (Kleinman et al. 2013)
173152+743615	262.968365	74.604272	3	16.60	5.9	C	p-l (one has large p and pm) + red inner component
173316+084954	263.31709	8.831643	2	17.78	2.4	C	similar colour p-l; companion has large pm
173509+094022	263.787393	9.672832	2	17.07	2.4	C	similar colour p-l; companion has large pm
173703+271724	264.262899	27.290003	2	18.37	2.5	C	similar colour p-l; companion has large pm
173820+041756	264.581302	4.298981	2	18.88	2.0	C	similar colour p-l; companion has large pm
173905+120306	264.77013	12.051664	2	17.77	2.8	C	similar colour p-l; companion has large pm
173915+112257	264.813269	11.382484	2	18.84	3.4	C	similar colour p-l; companion has large pm
174006+221101	265.024352	22.183576	2	17.45	1.8	C	similar colour p-l; includes $z = 1.406$ QSO (Healey et al. 2008); companion has large pm
174154+333616	265.474939	33.604416	3	16.54	8.5	C	p-l; outer components have large p and pm
174213+402717	265.55245	40.454758	2	18.30	3.1	C	similar colour p-l; companion has large pm
175243+093822	268.179389	9.639313	2	18.29	2.6	C	similar colour p-l; companion has large pm
175826+191732	269.608868	19.292361	2	17.57	2.5	C	similar colour p-l; companion has large pm
180257+244143	270.737205	24.695406	3	17.27	4.3	C	similar colour p-l (one companion has large pm) + red central component
180901+160103	272.254121	16.017515	2	18.59	3.1	C	similar colour p-l; companion has large pm
181045+742546	272.686785	74.429515	2	18.39	2.0	C	similar colour p-l; companion has large pm
181400+705410	273.499637	70.902881	2	17.69	2.4	C	similar colour p-l; companion has large pm
182159+275657	275.494183	27.949111	2	18.43	2.4	C	similar colour p-l; companion has large pm
182301+500140	275.753046	50.027664	2	17.91	2.0	C	similar colour p-l; companion has large pm
183204+491637	278.015957	49.276889	2	18.06	1.9	C	similar colour p-l; companion has large pm
183852+520350	279.718445	52.063814	2	18.13	3.1	C	p-l; companion has large pm
183916+454103	279.818168	45.684238	2	18.70	3.0	C	similar colour p-l; $4C\ 45.38, z = 0.958$ QSO; companion has large pm
184256+442102	280.733259	44.350567	2	18.33	3.1	C	similar colour p-l; companion has large pm
185008+441126	282.533367	44.190435	2	17.64	2.7	C	similar colour p-l; companion has large pm
185824+475553	284.600174	47.931329	3	18.54	3.6	B	p-l (one component has large pm), red inner component
190033+522319	285.012245	52.388677	3	18.18	2.8	C	similar colour p-l (one component has large pm) + red inner component
190433+575031	286.139132	57.841829	2	19.00	3.2	C	similar colour p-l; companion has large pm
192457+492126	291.239533	49.357218	2	18.71	2.8	C	similar colour p-l; companion has large pm
195629–064134	299.121219	–6.692813	2	19.12	1.6	C	similar colour p-l; companion has large pm
200550–030100	301.456704	–3.016733	2	18.49	3.7	C	similar colour p-l; companion has large pm
201810–022908	304.540147	–2.485511	2	18.25	1.8	C	similar colour p-l; companion has large pm
202339–290706	305.91091	–29.1182	2	17.93	2.0	C	similar colour p-l; companion has large pm
203106–122005	307.776472	–12.334677	3	17.59	3.1	C	similar colour p-l (one component has large pm) + red companion
204541+122718	311.419538	12.454995	2	17.86	3.0	C	similar colour p-l; companion has large pm
204628–20049	311.615311	–12.01355	2	19.12	1.9	C	similar colour p-l; companion has large pm
210519+161334	316.330544	16.226221	2	18.71	1.7	C	similar colour p-l; companion has large pm

Table B1 – continued

Name (PS1 J...)	$\alpha$	$\delta$	#Comp	$i$	Sep. (arcsec)	Rank	Notes
210820+122340	317.08394	12.394343	2	17.89	1.8	C	similar colour p-l; one component has large p
211017+050707	317.571284	5.118593	2	18.60	2.8	C	similar colour p-l; companion has large pm
211945+153713	319.938477	15.620234	2	17.58	2.9	C	similar colour p-l; companion has large pm
212755+085302	321.972353	8.883872	2	18.50	2.2	C	similar colour p-l; companion has large pm
213147+030935	322.946983	-3.159735	3	18.52	6.9	C	similar colour p-l (one has large pm) + extended inner component
213707+124621	324.279402	12.772593	2	18.67	1.8	C	similar colour p-l; BL Lac (D'Abrusco et al. 2014); companion has large pm
214102+265252	325.257922	26.881249	2	17.78	2.8	C	p-l; companion has large pm
214210+255233	325.543115	25.875914	2	16.95	2.4	C	similar colour p-l; companion has large pm
214248+290427	325.698926	29.074187	2	17.38	3.6	C	similar colour p-l; X-ray source (D'Abrusco et al. 2014); companion has large p and pm
214605+264507	326.52051	26.75202	2	19.2	2.3	C	similar colour p-l; companion has large pm
215502+190303	328.756839	19.050739	2	16.86	2.1	B	similar colour p-l; QSO+star (NTT run 0100_A-0297(A), PI. T. Argueta)
220822-142722	332.093734	-14.455987	2	17.25	2.1	C	similar colour p-l; companion has large p and pm
222238+354225	335.656449	35.707081	2	18.30	2.1	C	similar colour p-l; companion has large pm
222611-282413	336.547769	-28.403508	2	19.18	2.7	C	similar colour p-l; includes $z = 0.016$ galaxy (Maddox et al. 1990); companion has large pm
223604+221604	339.015242	22.267863	2	17.98	3.1	C	similar colour p-l; companion has large pm
223713+245120	339.304497	24.85563	2	18.26	1.7	B	similar brightness p-l + extended? HS 2236+1344 (blue compact galaxy); both have large AEN, no other
223831+140027	339.629583	14.007554	2	19.50	3.1	B	similar colour p-l + extended? HS 2236+1344 (blue compact galaxy); both have large AEN, no other
230258-281314	345.740301	-28.220566	2	18.24	1.7	C	<i>Gaia</i> data
231209+203543	348.036702	20.595139	2	19.16	3.1	C	similar colour p-l; companion has large pm
231313+194722	348.302961	19.7895	2	17.63	3.2	C	similar colour p-l; companion has large pm
231445+303530	348.687176	30.591695	2	17.20	3.0	C	similar colour p-l; companion has large p and pm
232837+435308	352.152836	43.885431	2	17.33	2.1	B	similar colour p-l; companion has large pm
233611-093523	354.043989	-9.589647	2	15.63	4.1	C	similar colour p-l; companion has large p and pm
233700+180520	354.249022	18.088753	2	17.63	3.7	C	p-l; companion has large pm
234155+32902	355.480568	13.483904	2	18.82	3.2	C	similar colour p-l; includes SDSS $z = 0.729$ QSO; companion has large pm
235351-053956	358.462667	-5.665505	3	16.5	6.2	B	similar colour p-l (companion has large p and pm) +red inner component; QSO+star (Williams et al. 2017)

The systems above the horizontal line are confirmed lenses or quasar pairs. The ones below are candidates ruled out either due to their *Gaia*-based properties, or due to spectroscopic results from the literature. The table structure is the same as in Table 1. ‘NIQ’ stands for nearly identical quasars.

This paper has been typeset from a *TeX/LaTeX* file prepared by the author.